Analysis of Diodes at Cryogenic Temperatures in an Ultra-High Vacuum

written by

Timo Wittler

Bachelor Thesis in Physics

submitted to the

Faculty of Mathematics, Computer Science and Natural Sciences of the RWTH Aachen University

in November 2022

at the

Physics Institute III. A

First Supervisor: Prof. Dr. Thomas Hebbeker
Secondary Supervisor: Prof. Dr. Achim Stahl

Contents

1 Introduction

To gain further insight into the nature of the universe, it is possible to explore new information sources like gravitational waves (GWs). The detection of GWs by aLIGO[1] in 2015 proved that this new way of looking at the universe is possible [1]. The Einstein Telescope (ET) will be part of the third generation of GW interferometers, which is currently being developed.

Since the amplitude of such waves is very small, the setup has to be very sensitive to changes in length and therefore to vibrations, which is why a vibration-isolation system is necessary. A part of this system are the so called OSEMs[2] [2]. Due to the cryogenic temperatures in which the low frequency part of ET is going to operate, the behavior of the OSEMs diode needs to be analysed and characterized. The goal of this thesis is the temperature dependence analysis of different LEDs in an ultra-high vacuum (UHV) in a temperature range of a few Kelvin to room temperature.

1.1 Basics of Gravitational Waves

In 1916 Albert Einstein predicted the existence of GWs as a solution of his general theory of relativity [1]. GWs are transversal spacetime waves that propagate with the speed of light [3]. That makes them fundamentally different from other waves such as electromagnetic (EM) waves, which travel through spacetime. That is why GWs are often referred to as "ripples" in spacetime. Their sources are the most extreme events in the universe such as the merger of two black holes or two neutron stars [4].

Compared to EM radiation GWs are much harder to detect which is due to their small amplitude and the tiny effect they have on length differences. Nonetheless, the fact that they do not interact with matter itself makes them extremely valuable for research of inner processes of stellar objects and events [5].

1.2 Interferometric Gravitational Wave Detectors

The design of a ET is based on the principle of Michelson interferometers as shown by the example of LIGO in Figure 1 [6]. The Laser emits monochromatic light with a particular wavelength that is split up by the beam splitter, which results in two partial light beams that are orthogonal to each other. The beams then propagate into the arms of length L. In real GW detectors, the light is passing through a cavity of length L thousands of times before exiting resulting in a longer effective arm length of the detector [7]. At LIGO the cavities with a length of $L = 4\,\mathrm{km}$ increase the sensitivity to small changes in length by a factor of approximately 140 [8]. After exiting the arms, the EM waves are recombined by the beam splitter, interfere with one another and hit a photodiode (PD).

The effect of GWs on the PD is described via the strain, which is the relative length difference $\Delta L/L$. ΔL is the change of distance between two points in space

---

[1]**aLIGO**: **a**dvanced **L**aser **I**nterferometer **G**ravitational-Wave **O**bservatory
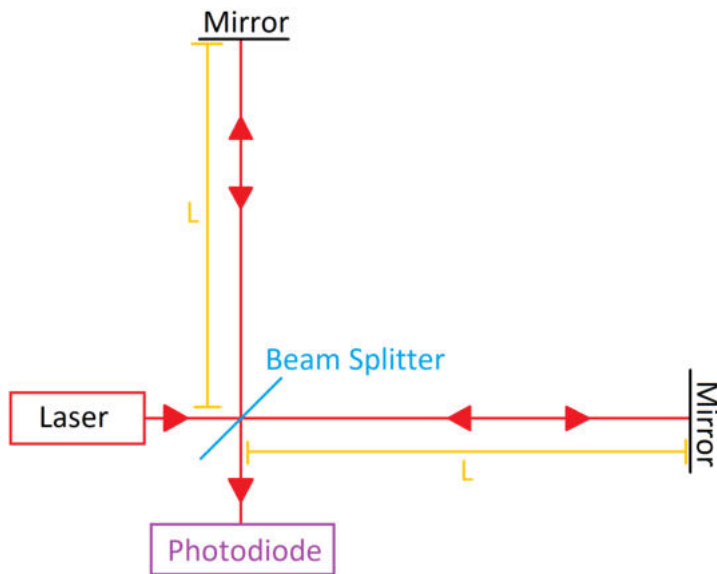[2]**OSEM**: **O**ptical **S**ensor and **E**lectro **M**agnetic actuator

Figure 1: Basic principle of a Michelson interferometer. The Laser emits monochromatic light that is split up by the beam splitter. The two partial beams propagate through the arms with length L and get reflected by the mirrors. The beam splitter then recombines the beams, which results in their interference. After that, the light is detected by the photodiode. In reality this setup is more advanced and complicated, but the basic idea stays the same.

while a GW is passing through them and L describes the length between the points without the wave.

The strain amplitude of the first measured GW had a maximum of 10^{-21} and was send out by the merger of two black holes [1]. Thus, the first generation (1G) of telescopes such as LIGO, VIRGO, TAMA 300 or GEO600 were just not sensitive enough to measure such an event. This changed with the second generation (2G) and detectors like aLIGO, aVIRGO and KAGRA[3] and their direct measurement of GWs. In the future, the goal is not to only detect GWs but to gather information about their origin from these waves.

The third generation (3G) of GW detectors is now being developed with projects like ET and Cosmic Explorer (CE). As visible in Figure 2, ET will have 10 to 100 or more times less noise strain than its predecessor aLIGO, depending on the frequency. Note that the unit $\mathrm{Hz}^{-1/2}$ is a result of the spectral amplitude density which is a scaled Fourier transformation, and the curve for ET is for a single detector and an angle of 90° between the arms to be able to compare the different layouts [9]. It is also important to keep in mind that the polarization (not for the current ET design [9]) and the direction of the wave might decrease the sensitivity of the detector, which is shown in Figure 2 by different shades of colors. It is also visible that the high and low frequency ranges of the different detectors overlap at about $12\,\mathrm{Hz}$, which explains the small increase. We will go into more detail about the different frequency ranges later. The peaks in the strain curve of ET are a result of the

---

[3]**KAGRA**: **Ka**mioka **Gra**vitational Wave Detector

suspension noise and its resonance.

The increased sensitivity of 3G detectors allows a better localization of objects and events that benefits multi-messenger astronomy too. For instance, a black hole merger could first be detected and localized by a GW observatory, which other telescopes use to gather further information from EM waves in the same location.
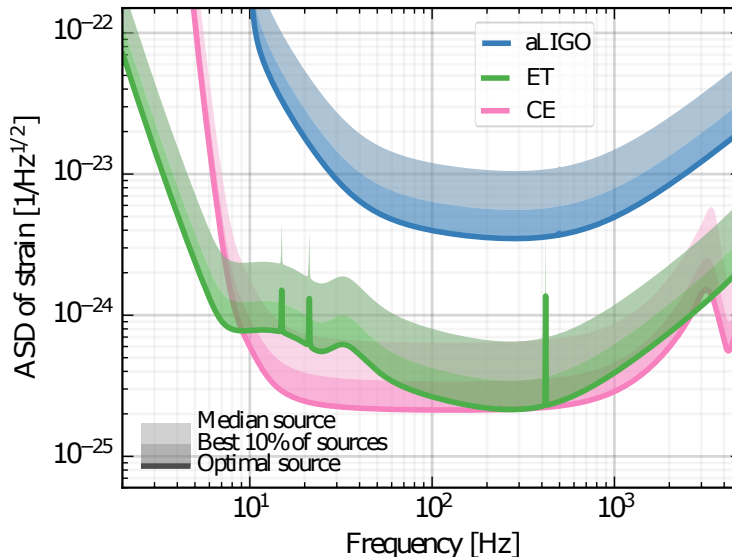

Figure 2: Noise strain comparison of aLIGO, ET and CE [9]. The various color shades indicate different source locations and orientations. Due to their small noise strain, the 3G detectors will be 10 to 100 or more times sensitive than aLIGO. The visible peaks of the ET curve are a result of the suspension resonance that occur at specific frequencies depending on factors like the used material and its shape. The small increase at approximately 12 Hz can be explained by the overlapping of the high and low frequency detectors of ET.

1.3   Einstein Telescope

ET will to improve the sensitivity significantly. This is only possible because of a few crucial design optimizations compared to 2G and 2G+ detectors like aLIGO. In order to achieve sufficient sensitivity at high frequencies, the light power in the arms has to be in the megawatt range. For low frequency detection on the other hand cryogenic optics are required, which is not feasible with a light power that high. This is why ET uses a so called "xylophone" design. The observatory is split up into two detectors, one optimized for low frequency measurements from 3 Hz to 30 Hz and one optimized for high frequency detection from 30 Hz to 30 kHz (illustrated by dashed and solid lines in Figure 3). Three interferometers will be installed for each detectors with an arm length of ten kilometers at an angle of 60° as shown in Figure 3. This design also allows GW detection independent of their polarization. We will focus on the low frequency interferometers in the following.

One of ETs goals is the detection of binary black hole coalescence up to cosmological distances. The project will also test several dark matter candidates and explore

the nature of dark energy which can have deep consequences on our understanding of the universe and its early stages [9]. To realize these goals, it is important to consider the noise reduction. As GW detectors are compared by their noise strain, the most consequential will be explained shortly.

In Figure 4, the total noise of low frequency and high frequency detectors are shown. Quantum noise is partly the result of Heisenberg's uncertainty principle that comes into play when the phase of light is measured very precisely. Another quantum noise effect is shot noise, which is an uncertainty that originates in the discretization of light particles. Since the light power falling onto the PD is made up of photons, a statistical error occurs in the data due to fluctuations of photon numbers hitting the sensor [9].
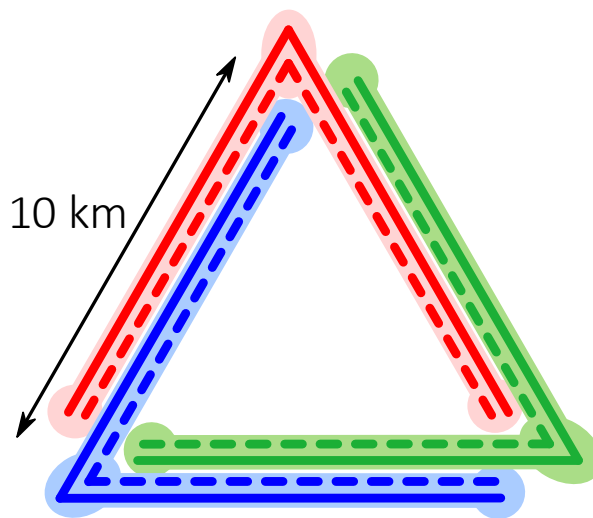

Figure 3: Basic outline of ET [9].

An important factor at low frequencies under 1 Hz is seismic noise, which is coupled into the system due to seismic activity in the region or other shaking of the earth, e.g. from human sources. The impact of seismic noise can be reduced by building the detector at a suitable, seismic calm location. In addition, ET will be buried at 200 m to 300 m under the surface. The advantage of such a location is the minimization of coupling via gravity gradients, which is caused by large amounts of moving mass that can have a gravitational effect on the suspensions and test masses, for instance by tides [9].

Thermal noise of the suspension and mirrors describes the movement of atoms and particles and has to be reduced especially for low frequencies. This is why the operating temperature of the low frequency arms will be in the range of 10 K to 20 K with a lower light power of 18 kW [9]. As shown in Figure 3, the thermal noise has peaks that are caused by the resonance of the suspension installed in the detector.

Another noise factor is excess gas which is due to the maximum pressure of 10^{-8} Pa $= 10^{-13}$ bar [9]. It can be reduced by using suitable materials like copper, stainless steel or ceramics and by minimizing the inner surface area of the vacuum vessel, so that water and other molecules can not adsorb [11].
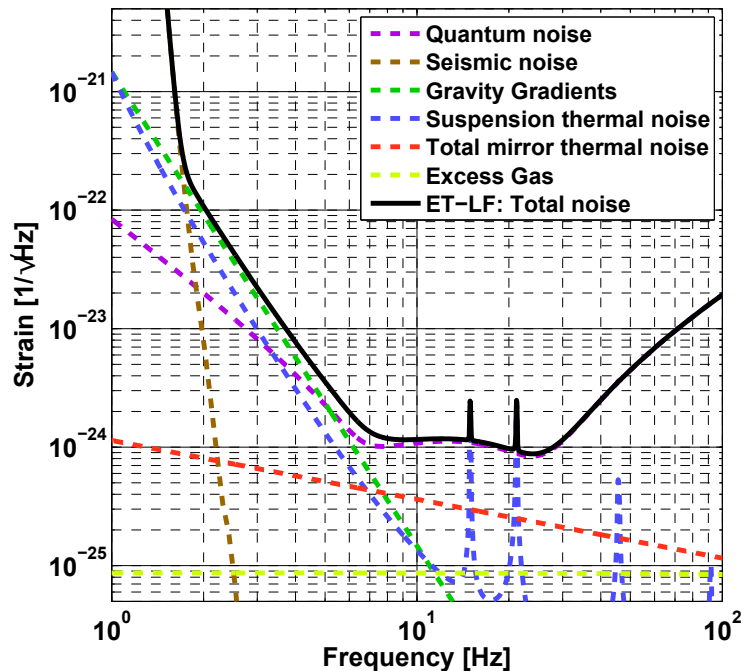
Figure 4: Total noise comparison of low frequency detector from [10]. The limiting noise factor at frequencies under 1 Hz is seismic noise.

1.4 Optical Sensor and Electromagnetic Actuator

The suspension of the test masses of ET is split into different stages that consist of passive and active damping parts. One component is an optical sensor and electromagnetic actuator (OSEM), which enables contactless position detection and correction. The design of the BOSEM[4] used at aLIGO is shown in Figure 5. The mounting of the device is a coilformer clamp to which the coilformer is fixed. The transmitting and receiving devices are located behind the clamp and are connected via a flexible circuit with an electrical interconnect. The transmitting end is a light emitting diode (LED) that emits light across a hole onto a PD, which is the receiving end. As shown in Figure 6, a flag protrudes into the light beam that crosses the hole. It is mounted onto a magnet, on which a force can be exerted via the actuator. The actuator consists of a coil that is able to exert a force onto the magnet via a current.

The LED, PD and flag form the shadow sensor that is used to detect the position of the flag. The PD voltage is monotonically increasing with an increasing light power which is proportional to the area the flag is covering. In a certain range the monotone rise of voltage can be approximated by a linear function to determine the displacement of the flag [2]. This is how the position can be measured precisely without contact. As visible in Figure 6, the LEDs beam is also propagating through a lens to get a beam profile that is as uniform as possible, since a non-uniform profile could distort the linear response of the PD [2]. This is the case for the BOSEM installed at aLIGO too.

The thermal connection of the carriers to the LED and PD has to be good as the

---

[4]**BOSEM**: **B**irmingham **O**ptical **S**ensor and **E**lectro **M**agnetic actuator
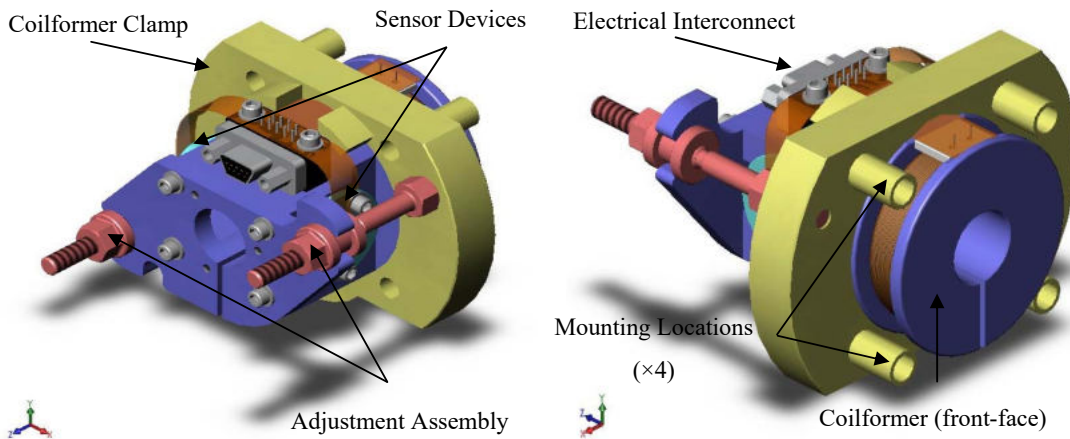
Figure 5: Isometric view of the BOSEM design [12].

major way of heat transportation in the cryostat is conduction. The LED produces a significant amount of heat during operation at low temperatures that has to be able to conduct to not heat up other components of the system.

It is important to know the behavior of the used LEDs at cold temperatures. This thesis treats the analysis of LED candidates for the transmitting end that is required for an OSEM.

1.5 Light-Emitting Diodes

To understand the effects temperature changes might have on the LEDs, it is important to have a basic understanding of the underlying physics. The used diodes are made of semiconductors like GaAs [13] or GaN [14], which have properties that can be exploited to create LEDs. In the following, a broad overview of the mechanism that allows light to be emitted through semiconductors will be given.

1.5.1 Energy Bands

Since the electrons in a material interact with each other over many atomic distances, the discrete energy levels of the individual atoms merge into energy ranges, the so-called energy bands. There are two main bands: the conduction and the valence band. The conduction band consists of higher energy levels than the valence band and is therefore responsible for conduction. For metals they overlap so that they conduct as shown in Figure 7. This means that the conduction of electrons does not require energy to bridge the band gap, as is the case with isolators and semiconductors. In the latter they can be excited by a small amount of energy into the conduction band. Typical values of energy band gaps are $1.42\,\text{eV}$ for GaAs or $3.39\,\text{eV}$ for GaN. In Figure 7 the lowest energy state of the conduction band is called E_C and the highest energy of the valence band is named E_V. The band gap E_g can therefore be calculated via $E_g = E_C - E_V$ [15].

In isolators on the other hand, the energy required to excite an electron from one band into the other is too high for normal applications so that the conductivity is effectively zero. The Fermi energy or electrochemical potential E_F in Figure 7 is
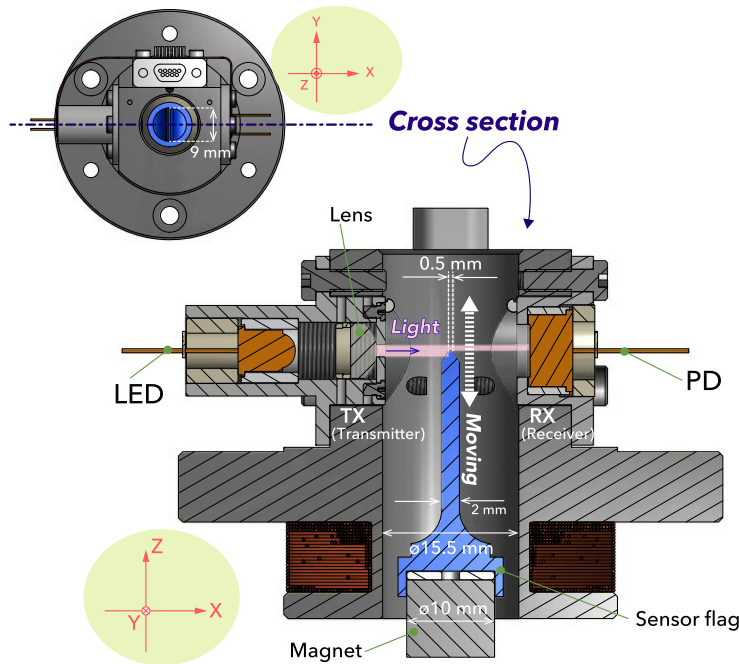
Figure 6: Schematic side view of the OSEMs functional parts adapted from the design review of KAGRA [2]. The system applied at ET will differ from this approach.

defined as the maximum energy that a system in its ground state is able to occupy [16].

For semiconductors, the transport of electrical current is only possible at temperatures $T > 0\,\text{K}$. This is due to the fact that only partial occupied bands are able to conduct, which is only the case at non-zero temperatures, because of thermal excitation. To increase the conductivity further, it is possible to dope the semiconductor substance. when a material is doped, different types of atoms (impurities) are pot into it to increase its charge carrier concentration. Atoms with one electron more than the semiconductor atoms add free electrons, while atoms with one electron less add holes. These holes can be described the same as electrons, but with a positive charge. The materials are named n-doped and p-doped semiconductors, respectively. Note that both materials on their own are electrically neutral [15].

1.5.2   PN-Junctions

When the p- and n-doped materials are joined, a pn-junction is created. It can be split into three main regions: the n- and p-region plus the depletion region between them [17, p. 452]. There is an imbalance of carrier concentration between the doped regions due to different Fermi energies. The charge carriers diffuse into the other region where they recombine. This diffusion current creates an electric field, which exerts a force on the charges that is opposed to the "diffusion force". When these forces are the same, an equilibrium is achieved. This is the case when the different Fermi levels align [18]. The energy band diagram of a pn-junction is shown in Figure 8. The Fermi energy in the pn-junction is constant, while E_C and E_V fade into each other in the depletion region. Since some electrons and holes diffused into
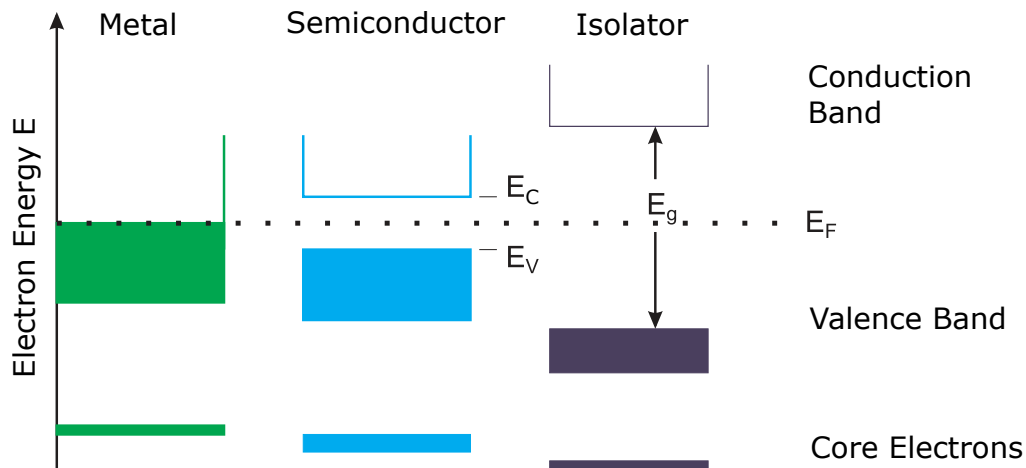
Figure 7: Schematic view o the energy bands in different material types adapted from [15, p. 104]. The band of metals overlap so that free charge carriers are able to conduct without an excitation energy. Semiconductors have a small band gap between the valence and the conduction band. The Fermi energy lies in the middle of this band gap for ideal, pure materials [15, p. 104]. As impurities are added to the material, it is shifted up or down toward the bands. The band gap energy has an order of magnitude of eV.

this region, the n-, p- and depletion region are no longer electrically neutral. The material as a whole stays neutral as it is a closed system.

Now one can apply a voltage to the pn-junction with the negative pole at the p-region and the positive pole at the n-region, which results in no measurable current. This is due to holes in the p-region getting attracted by the positive pole away from the depletion region, while the electrons in the n-region do the same towards the negative one. An increasing width of the depletion region follows, so no current can flow[5]. If the poles are switched, the width of the depletion region decreases, since the electric field resulting from the applied voltage is opposed to the field in the region. Now the diffusion current increases, because the potential hill of the depletion region is less steep. If the voltage is now raised slightly, the flowing current increases exponentially [19, pp. 3–4]. An equilibrium is not achieved anymore, since the recombined charges are replaced by charge carriers from the voltage source. This property of semiconductor materials is a requirement for light to be emitted by the pn-junction.

1.5.3 Light Emission

The pn-junction is able to emit light, if the material is a direct semiconductor. This means that a energy minimum of the conduction band lies over a maximum of the valence band [20]. The electrons and holes in the depletion region recombine and emit photons with a particular wavelength, which is specific for every material

---

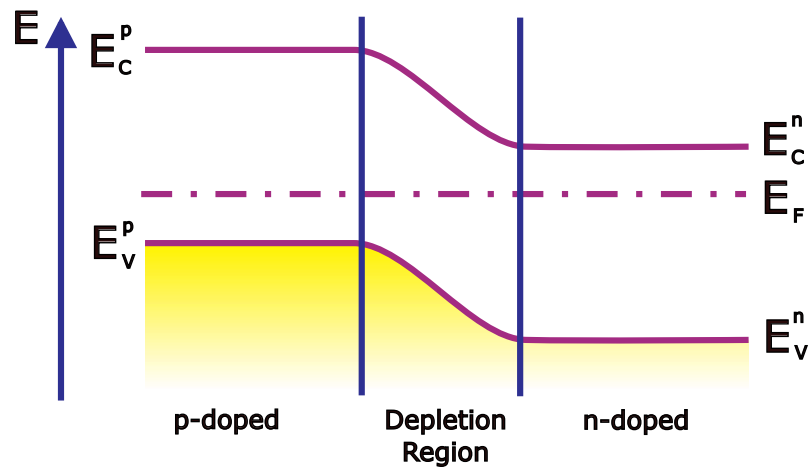[5]In reality a small leakage current can be measured.

Figure 8: Simplistic energy band diagram of a pn-junction from [15, p. 124]. The Fermi energy is constant, while the valence band and the conduction band energy blend into each other.

composition [21]. This is due to the different energy levels that are occupied in the different bands. Since their occupation is temperature dependent too, the diode output should depend on the temperature. For instance, high temperatures yield more occupied states at high energies, while only energies up to the Fermi level are occupied for $T = 0$. Another temperature dependent factor is the electron mobility μ, which is defined as the coefficient between a given electric field and the resulting drift velocity of electrons. The band gap energy is also conditional to temperature. A discussion of the reasons behind the measured LED temperature dependence will be given in the analysis part.

2 Setup and Calibration

The system used to measure the LEDs temperature dependence consists of two components: a vacuum chamber and a cryostat. The vacuum chamber is able to sustain an ultra-high vacuum with pressures below 10^{-8} hPa. The cryostat cools the components inside the vacuum chamber to temperatures below 10 K. The devices used to achieve this environment and measure the important parameters will be explained now.

2.1 Vacuum and Cryostat Setup

The used setup is visible in Figure 9. The customized vacuum chamber is made out of thick stainless steel in a cylindrical shape with a diameter of 20 cm, which is mounted onto a frame [22]. It has different flanges with feedthroughs to connect required devices. To achieve the desired pressures under 10^{-8} Pa, a Turbopump from Pfeiffer Vacuum is installed (Figure 9 (a)). It is cooled by a HIPACE Aircooling. The power supply is provided by a TPS 310 Power Supply Pack, while the pump is controlled by TC 110 Electronic Drive Unit that is fixed onto the pump. To reach a pre-vacuum, which is needed for the Turbopump to start, a MVP 030-3 DC Diaphragm Pump is connected.
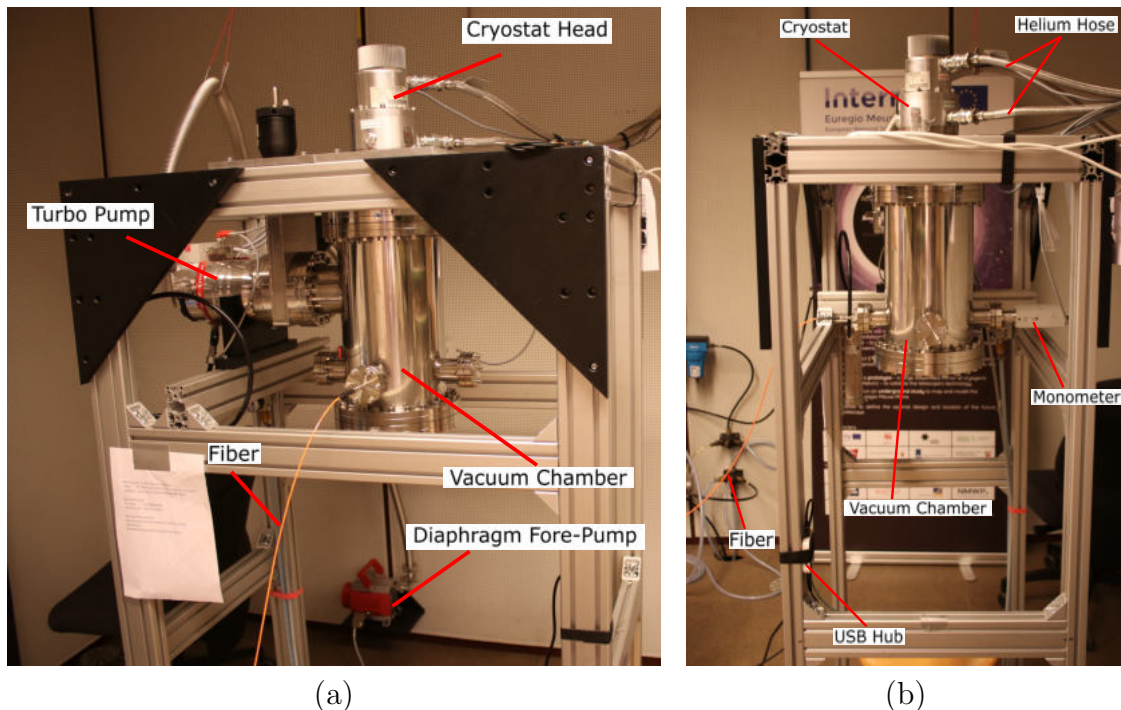

(a)   (b)

Figure 9: Vacuum chamber with cryostat mounted on top.

To measure the pressure, a PBR 260 Compact FullRange BA Gauge is mounted on the side of the chamber (Figure 9 (b)). The temperature is measured by a Model 335 Temperature Controller from Lake Shore Cryotronics. The cryostat head is placed on top of the vacuum chamber and is supplied with liquid helium via two hoses. The hoses are linked to a water-cooled HC-4E Compressor.

The cylindric sample volume inside the vacuum chamber has a height and diameter of 15 cm. The cooling plate of the cryostat forms the upper end of the cylinder, while a heat shield is located at the bottom and around the volume. The LED is connected to the cooling plate via two copper heat links, as shown in Figure 10 (a). A copper lid holds the LED in its place and is fixed on top of it with two screws. One of the other holes on the side, visible in Figure 10 (a), is used to put a temperature sensor on the mounting. The last one is a venting hole to prevent fake leaks while pumping a vacuum. The used copped here is oxygen-free copper (OFC).
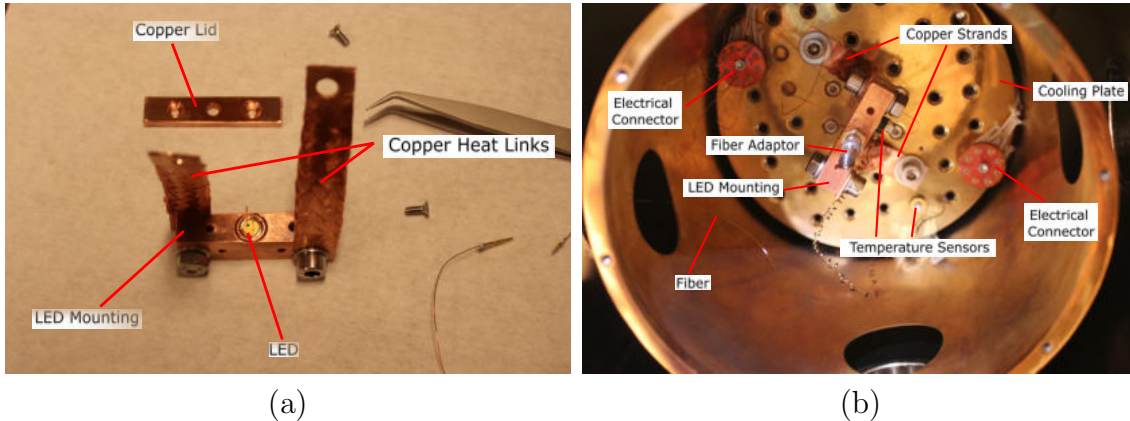

(a)   (b)

Figure 10: (a) Copper mounting of the LED: The lid will be screwed ontop of the LED between the heat links fixing it in place. Another hole on the side is cut into the copper to attach a temperature sensor. (b) Cylindric sample space with the LED inside its mounting. It is connected via the electrical connector to a power supply outside of the vacuum chamber. The emitted light is collected by the optical fibre and is directed outside through a flange with fibre connection. Two temperature sensors are installed: one on the cooling plate and one on the LED mounting.

It is very important to have a good thermal connection between the cooling plate and the LED. OFC has a high thermal conductance and is vacuum compatible, which is why it is used here. The LED inside the mounting emits light that is collected by the optical fibre and propagates through a flange to a fibre outside of the vacuum chamber. In most cases, the fibre inside the chamber has a diameter of 200 µm. The LED is powered via the electrical connection (see Figure 10 (b)) by a current source outside of the chamber. The temperature sensors are also linked over this connection. Once everything is installed inside the sample space, the heat shield is mounted under the cylinder and the chamber can be closed.

Outside of the vacuum compartment, three different devices are used to measure the behavior of the LED. The temperature controller described above is used to collect the temperature data. The spectrum of the LED is gauged by an Red Tide USB650 Fiber Optic Spectrometer from Ocean Optics. In Figure 11 a schematic view of the structure of this spectrometer is given. The fiber with a diameter of 400 µm, if not stated otherwise, is connected to the SMA connector (1). Light goes through a slit and a filter into the spectrometer (2-3). The latter restricts optical radiation to the pre-determined wavelength regions. The beam is then focused by a collimating mirror (4) onto a grating (5), which diffracts the light in different angles, depending on the wavelength. Another focusing mirror (6) reflects the spectrum onto

the sensor. The sensor is a Sony ILX511 Linear Silicon CCD Array Detector with a pixel size of $14\,\mu m \times 200\,\mu m$. Each pixel of the sensor (8) responds to the wavelength of light that strikes it, creating a digital signal. The signal is then transmitted to the computer that is collecting the data. (7) and (9) are optional filters that the used spectrometer does not have [23]. The spectrometer has a wavelength range from $400\,nm$ to $1000\,nm$.

The amount of light coming out of the fiber has an intensity that is too high for the spectrometer. This is why a reduction cylinder is put between the outside fiber and the spectrometer, which is shown in Figure 12. The tube is empty, so since the photons are not perfectly parallel to the fiber, some scatter against the tube wall. Most of the light still hits the beginning of the other fiber, which also has a diameter of $400\,\mu m$. This is only possible if the light in the beam is nearly equally distributed. To change the intensity reduction, the tube length can be varied. A longer cylinder means more light loss. The approximate length will be given for each LED separately.
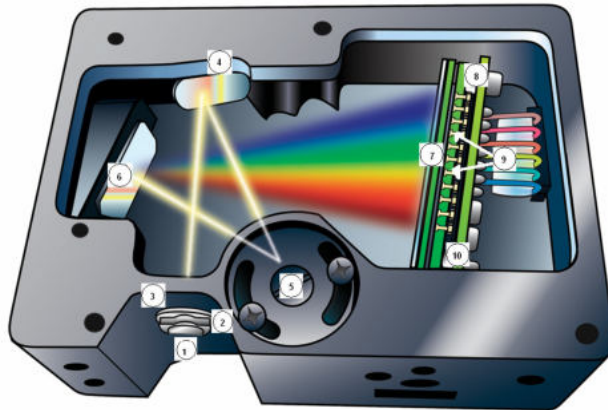

Figure 11: Schematic view of the spectrometer inlay from [23].

To power the LED, a PHILIPs PE 1514 voltage source is connected to a driver board. The two input voltages of the board provided by the voltage source are approximately $+18\,V$ and $-18\,V$. It is not that important to be exactly $\pm 18\,V$, since the driver board was designed to deal with a non-exact voltage source. It is based on a LIGO design that minimizes noise of the constant current supply of $35\,mA$. The output of the driver is connected to the LED. Its layout can be found in the appendix (Figure 43 and Figure 44).

The actual spectrum measurement is done by taking 100 spectra and averaging over each pixel to get a result that is not as prone to outliers. The forward voltage is averaged over 1000 data points and the temperature over 100 values. The statistical errors are logged too.

2.2 Calibration

A calibration of all used instruments is necessary. This section describes the calibration of the spectrometer, the current source and the ADC board.
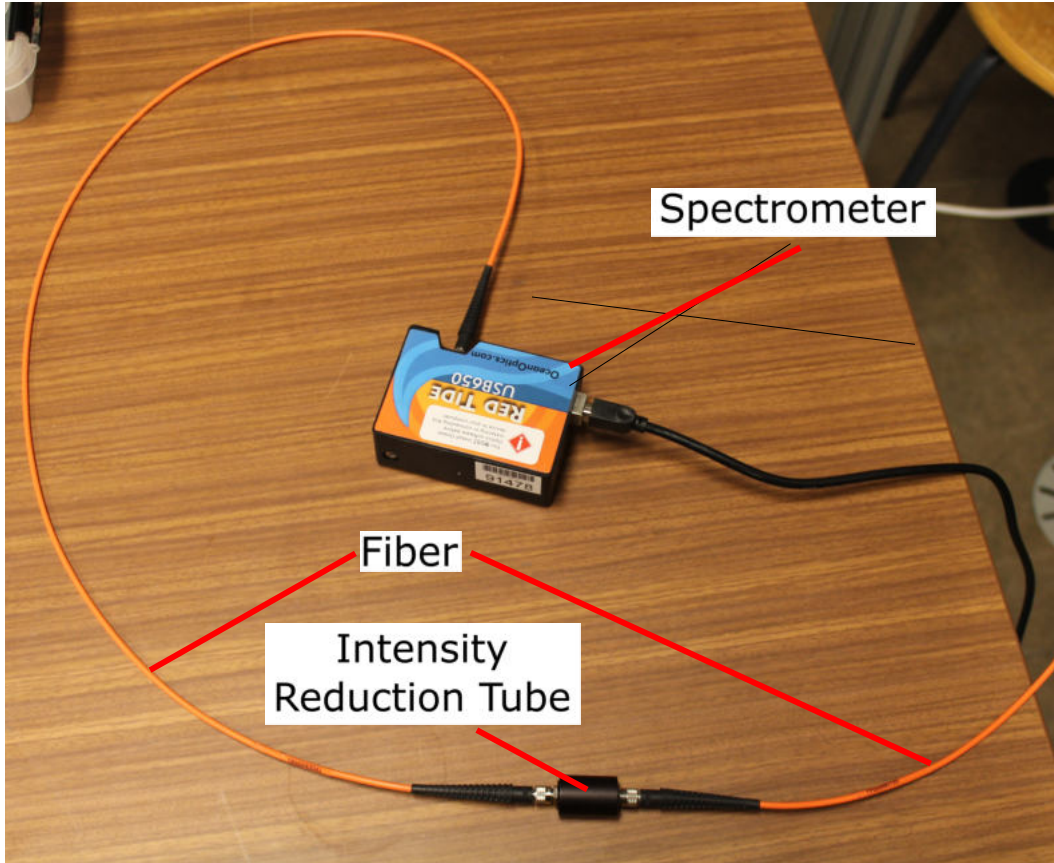
Figure 12: The used spectrometer and its connection via a fiber to the intensity reduction tube. The second fiber is connected to the vacuum chamber.

2.2.1 Spectrometer

A calibration of the spectrometer is required to convert the pixel of the spectrometer into wavelengths. The procedure is described in the spectrometers manual [23]. As visible in Figure 13, an argon gas discharge lamp is mounted in front of the fiber with a thickness of 400 µm. It is connected to a high voltage supply via wires. The emitted light propagates through an optical fiber to the spectrometer, where the digital signal is measured. The data is then transferred to a computer with SpectraLab[6] software that is able to save the spectrum as a text file. The used integration time[7] is 30 ms with a distance between the gas lamp and the fiber of approximately 0.5 cm. To achieve good results it, is necessary to measure in a dark room with as little light noise as possible.

SpectraLab converts pixel directly to wavelength, so the resulting plot has the wavelength on the x-axis. It cannot be assumed that the calibration of the program is correct, so a pixel value from 0 to 2047 is referred to each intensity point, since 2048 is the number of pixel in the spectrometer detector.

---

[6]Note that this software was only used to calibrate the spectrometer. Later spectra are taken by using the raw data from its output due to a different setup.

[7]The integration time of the spectrometer describes the time in which photons can hit the detector. An integration time of 30 ms means that the spectrum is measured for that long.
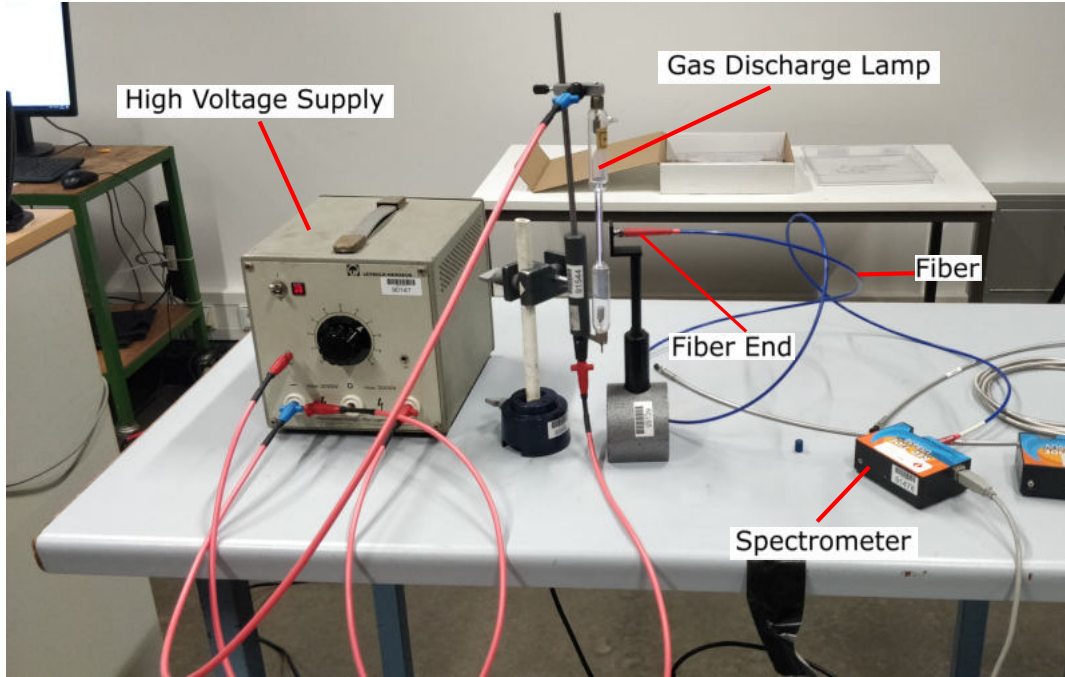
Figure 13: Setup of the spectrometer calibration. A argon gas discharge lamp is put in front of the $400\,\mu m$ thick fiber, which is connected to the spectrometer.

Assuming the wavelengths are distributed linearly, a scaling factor can be calculated:

$$p = k\lambda + p_0. \tag{1}$$

p is a pixel, λ the wavelength and k the scaling factor. Since the wavelength does not start at $0\,nm$, a pixel offset p_0 is introduced. Equation 1 is important for the error propagation later. k is calculated by inserting the highest and lowest wavelength into

$$k = \frac{\#p}{\lambda_{max} - \lambda_{min}}, \tag{2}$$

where $\#p$ is the number of pixel. This is a linear regression through the end points. p_0 can then be calculated by inserting a data point into Equation 1. The easiest point is where $p = 0$, which is at $\lambda = \lambda_{min} = 339.1\,nm$. λ_{max} is equal to $1027.8\,nm$. The resulting coefficients are $k = 2.9737 \pm 0.0002$ nm^{-1} and $p_0 = -1008.39 \pm 0.14$.

Additionally, an offset measurement is done by turning the gas discharge lamp off and record another spectrum. The two spectra are visible in the appendix (Figure 45 and Figure 46). To get an offset-free spectrum they are subtracted from each other. The resulting spectrum with its 15 used peaks is shown in Figure 14. To get the peak position and its intensity, each of these peaks is then approximated via a parabola with the form:

$$I(p) = a \cdot (p - b)^2 + c. \tag{3}$$

Here, I is the intensity and p is a pixel as before. a, b, c are coefficients that correspond to the slope, the peak position and the peak height, respectively. The peak is found by taking a small range around the peak where the fit is made. Since the peaks intensities are very sharp, it is only possible to get 5 to 6 data points

for each parabola, depending on the peak. The amount of degrees of freedom left is therefore very small. An example for the sixth peak is shown in Figure 15[8], which has a $\chi^2/N_{dof} = 1.67$, which is reasonably good. A full table of the fit parameters and the resulting peak position is visible in Table 8 in the appendix. For the intensity a statistical error of $\sigma_I^{stat} = 0.1/\sqrt{12}$ is assumed, since the resolution of the spectrometer is exact to 0.1 and a constant distribution between data points can be presumed. The wavelength difference of the wavelengths of SpectraLab is 0.4 nm. Therefore the statistical uncertainty of a wavelength measurement is set to $\sigma_\lambda^{stat} = 0.4/\sqrt{12}$ nm (also assuming a constant distribution between data points). This is due to the fact that a pixel can be hit by photons with slightly different wavelengths at different positions, since each pixel has a small, but significant size. Gaussian error propagation of Equation 1 gives a pixel error of $\sigma_{p,stat} = 0.085$. To consider both, the x- and y-error, the python module Orthogonal Distance Regression (ODR) is used.
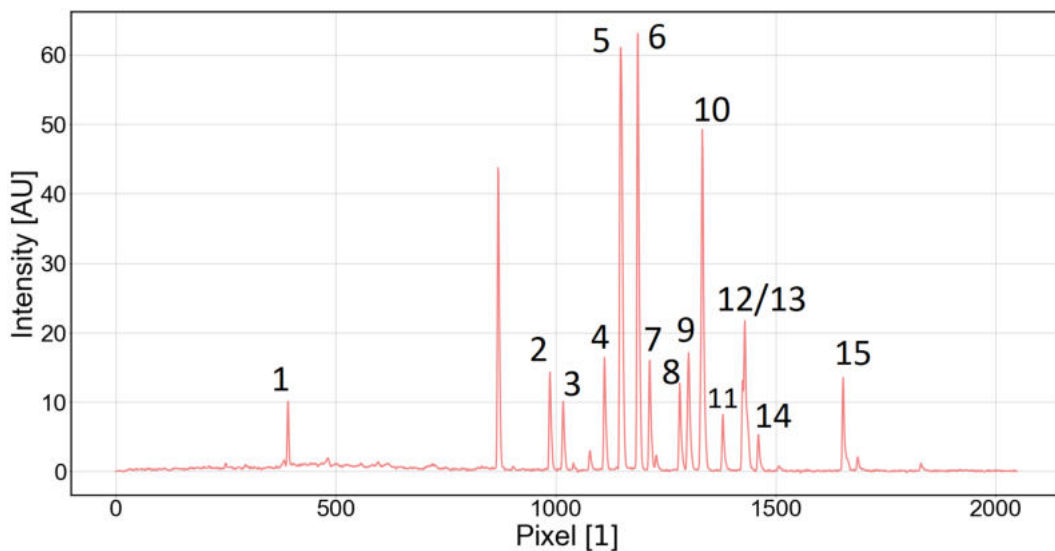

Figure 14: Argon spectrum with the 15 peaks used for calibration. Peak 12 and 13 are too close together be separated. The peak between peak 1 and 2 has an apex that is not gaussian but constant, which is why it is not considered here.

The peak positions are now being used to do get a cubic conversion formula $\lambda(p)$, where p is the pixel and λ the corresponding wavelength. To do so, the literature values of the argon spectrum are taken from [24]. A list of the values used for calibration is shown in the appendix in Table 8. The pixel can now be put on the x-axis and the wavelength on the y-axis. Now, each peak has a specific position in this 2D plane. According to the spectrometers manual [23], a regression with a cubic polynomial $\lambda(p) = ap^3 + bp^2 + cp + d$ is sufficient to describe the relation between a pixel and its corresponding wavelength. a, b, c and d are parameters that need to be calculated.

The resulting fit is visible in Figure 16 with the parameters in Table 1. The residual plot shows that the assumed errors on the wavelength and intensity are

---

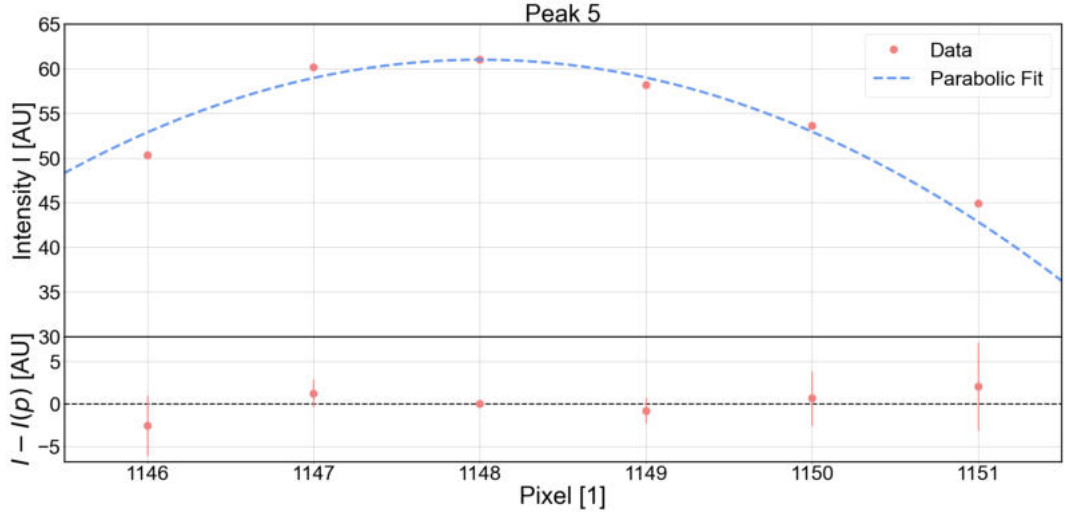[8]The other fits can be found in the appendix (Figure 47).

Figure 15: Example of a parabolic fit for peak 5 with residual plot. The statistical errors on the intensity and each pixel are $\sigma_I^{stat} = 0.1/\sqrt{12}$ and $\sigma_p^{stat} = 0.34$, respectively. The different errors for different pixel are a result of the error propagation of σ_p^{stat}. $\chi^2/N_{dof} = 0.84$.

$a \pm \sigma_a^{stat}$	$b \pm \sigma_b^{stat}$	$c \pm \sigma_c^{stat}$	$d \pm \sigma_d^{stat}$
$(-5.1 \pm 0.4)e - 9$	$(-0.5 \pm 0.1)e - 5$	0.363 ± 0.001	347.8 ± 0.3

Table 1: Fit parameters of the cubic fit (Figure 16).

.

reasonable. This is supported by a χ^2/N_{dof} of 4.82. Now a raw spectrum taken by the spectrometer, which is pixel dependent, can be calculated into one that is wavelength dependent.
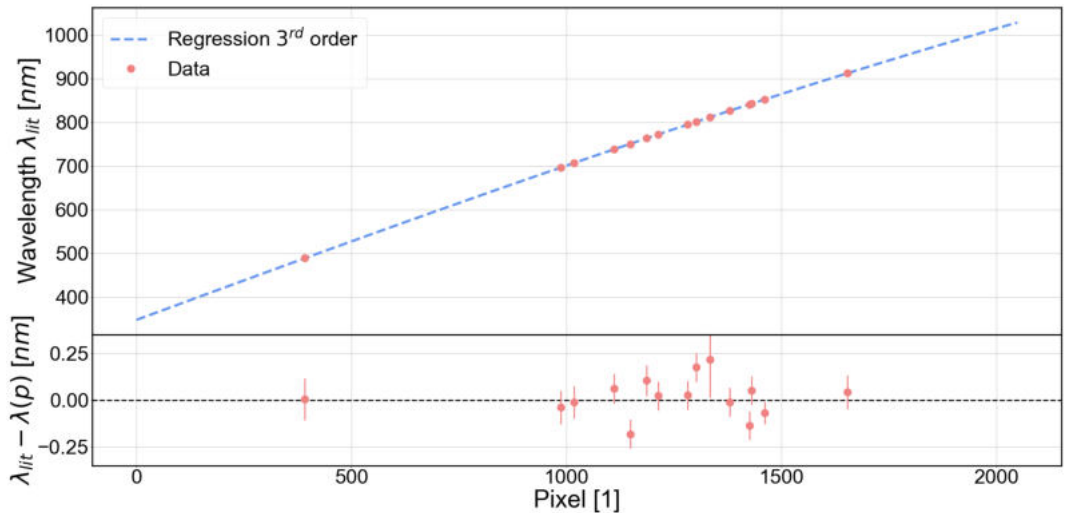

Figure 16: Cubic regression and corresponding residual plot for the spectrometer calibration. $\chi^2/N_{dof} = 4.82$.

2.2.2 Current Source

To calibrate the current source, different resistances are connected to its output. An Agilent 34401A Digital Multimeter is put in series to measure the current. The chosen resistances have a value between $33\,\Omega$ and $304\,\Omega$, since the expected current is around $35\,$mA and the forward voltage will be in the range of $1\,$V to $9\,$V. The resistance is then calculated by Ohms law $R = U/I$. A list of the used resistances is shown in Table 2. Since their actual value is not important here and the resistance is measured more precisely than the value given by the supplier, no uncertainties on the resistances are given.

Resistance $R\ [\Omega]$	33	39	51	62	82	91	110	112	121	137
	151	180	193	212	237	259	270	290	304	

Table 2: Resistance values for the current source calibration.

The voltage is measured by using a METEX M-3630 Multimeter. Since a voltage measurement could have an effect on the current results, the voltmeter is disconnected for each current recording. The voltage across the resistor is then measured with the voltmeter. The resulting I and V values seem to have a linear relation, which is why a linear function $I(V) = mV + b$ is fitted to them. The plot shown in Figure 17 confirms that assumption. The gray line shows that two measurements were made at different times due to an unexpected high forward voltage of the MTE4064NK2-UR LED (see section 3). The different measurements are compatible with one another.
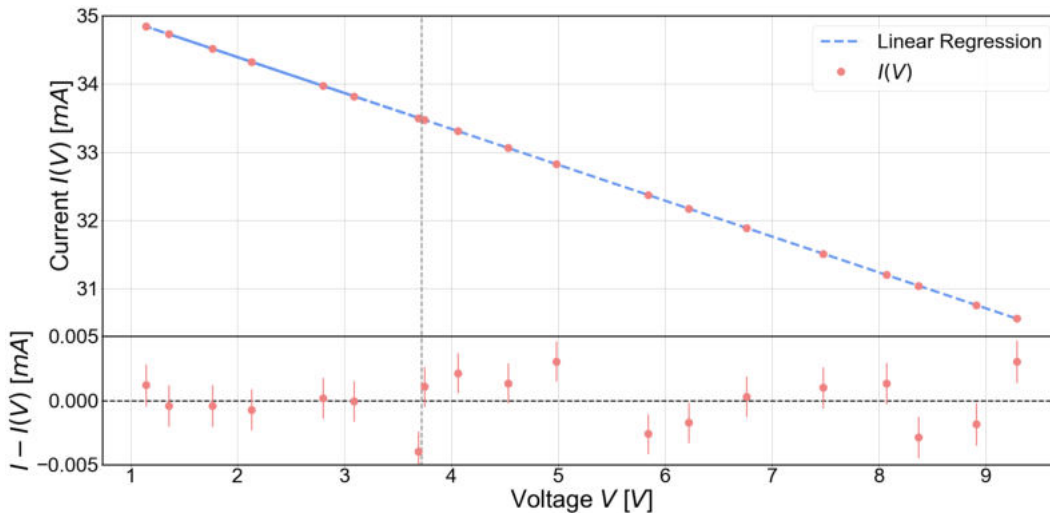

Figure 17: Current source calibration fit. The gray line shows that two different measurements were used. $\chi^2/N_{dof} = 0.73$

It seems that the current source is actually not as constant as expected. This is probably due to a diode on the board, which has a leakage current that is proportional to the voltage. The systematic errors on the current are taken from [25]: $\sigma_I^{sys} = 0.010\% \cdot I + 0.004\% \cdot I_R$. $I_R = 100\,$mA is the current range set on the

multimeter and I is each current value. Since the voltmeter does not have a data sheet, an estimation of a relative systematic uncertainty of $\sigma_V^{sys}/V = 5\%$ is made, since it is old and probably not calibrated that well anymore. The statistical errors originate in the resolution of each multimeter. A constant distribution between the data points is assumed: $\sigma_I^{stat} = 0.0001/\sqrt{12}$ mA, $\sigma_V^{stat} = 0.01/\sqrt{12}$ V. The fit in Figure 17 uses the statistical errors. The resulting coefficients are shown in Table 3.

$m \pm \sigma_m^{stat}$	$b \pm \sigma_b^{stat}$	χ^2/N_{dof}
-0.5260 ± 0.0001	35.445 ± 0.001	1.75

Table 3: Coefficients of linear regression using statistical uncertainties.

The propagation of systematical errors is done by the "shift method". The assumed uncertainties are added once and subtracted once from each data point. Since there is an error on the voltage and on the current, this yields four different set of points with I_+, I_-, V_+ and V_-[9]. For each set, a linear approximation with the statistical errors is done. The systematic error is then given by the maximum difference Δ_{max} between the coefficients resulting from the fit in Figure 17 and the coefficients coming from the shifted fits. The results are shown in Table 4. A plot of the used shift method can be found in the appendix (Figure 48).

	$m \pm \sigma_m^{stat}$	$b \pm \sigma_b^{stat}$	χ^2/N_{dof}
I_+	-0.5260 ± 0.0001	35.4529 ± 0.0008	1.75
I_-	-0.5259 ± 0.0001	35.4378 ± 0.0008	1.75
V_+	-0.5009 ± 0.0001	35.4454 ± 0.0007	1.93
V_-	-0.5537 ± 0.0002	35.4454 ± 0.0008	1.58
Δ_{max}	0.028	0.0075	

Table 4

The complete coefficients resulting from the calibration are ($k \pm \sigma_k^{stat} \pm \sigma_k^{sys}$):

$$m = -0.5271 \pm 0.0007 \pm 0.0277 \; \frac{mA}{V}$$
$$b = 35.4474 \pm 0.0016 \pm 0.0075 \; V$$

They can now be used to get a realistic current value $I = mV + b$, which depends on the measured voltage.

2.2.3 ADC Board

The ADC board can be calibrated by measuring the forward voltage of a LED not only with the board itself, but also with a multimeter. This was done with an OP232

---

[9]I_+ for instance, describes the set of points where V is the same, but the systematic error is added to current values. This is done analogically for each error.

LED. The used multimeter is, as for the current source calibration, the Agilent 34401A Digital Multimeter. While cooling down the cryostat, the forward voltage of the diode can be measured by switching the connection from the ADC board to the multimeter. This is done in-between the voltage measurements of the board. During the cooldown, the temperature difference that occurs while switching the wire is significant and has to be considered. The time between those measurements are typically around 10 s to 20 s. To evaluate the error, the voltage changes in this times are estimated. This was done during the start of the cooldown, where the temperature change is not that fast. It seems that a approximation of $\sigma_V = 1.5\,\mathrm{mV}$ is enough to cover this effect. This corresponds to a maximum relative error of $\sigma_V/V_{min} = 0.1\%$.

Although this is true for most cases, four data points will not be considered for the calibration, because the temperature change increases with lower temperatures (green points in Figure 18) and the time it takes to switch wires is too large to account for such an effect via an error. To minimize the uncertainty of the ADC counts, the board measures the forward voltage 1000 times and takes the mean value. The maximum resulting relative error is $\sigma_{c,rel}^{max} = 2.09e-4$ %, which is negligible compared to the other errors. In the following, the ADC board voltage will be called V_{ADC} and the multimeter voltage is V_{multi}.

Now, a linear regression $V(c) = mc + b$ between the ADC counts and the multimeter voltage can be done. $V(c)$ is the resulting voltage corresponding to a specific ADC count c. m and b are coefficients. The resulting curve is shown in Figure 18. The linear regression yields the parameters shown in Table 5. Since the χ^2/N_{dof} is close to 1, it is reasonable to believe that the process worked well.
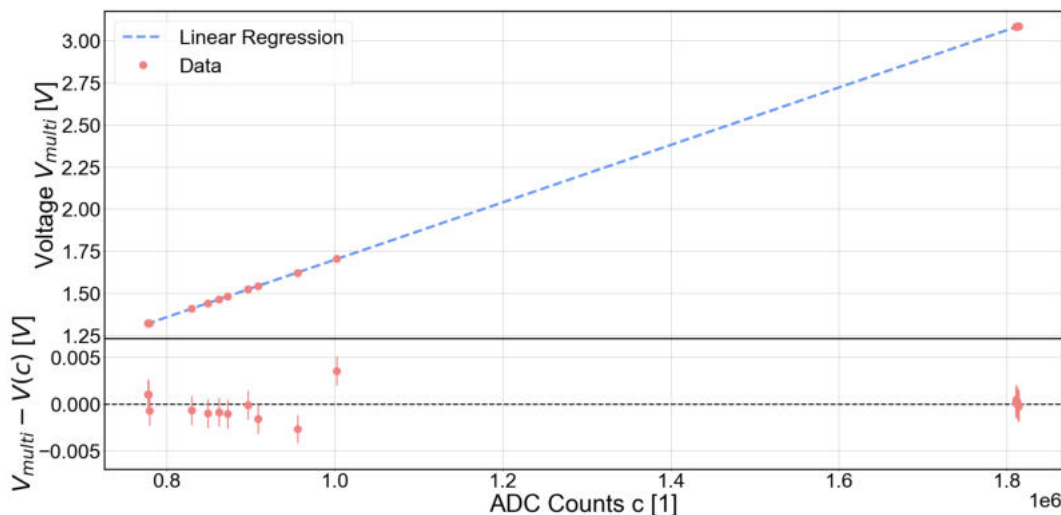

Figure 18: Linear regression curve of ADC board. $\chi^2/N_{dof} = 0.78$.

$m \pm \sigma_m$	$b \pm \sigma_b$	χ^2/N_{dof}
$(1.7040 \pm 0.0008)e-6$	-0.0049 ± 0.0009	0.78

Table 5: Fit parameters of the linear regression.

3   Analysis

To analyse the behavior of an LED, three main quantities are considered: the spectrum of the emitted light, the forward voltage of the LED and their corresponding temperature. The measurements use slightly different setups for data gathering, depending on the LED.

3.1   Spectral Intensity

Not all of the spectrometers pixel have the same sensitivity. This is why a sensitivity curve is given in [26] (see Figure 49). Since the curve is only accessible in the data sheet, it has to be approximated. A manual cursor is used to gather data points that describe the curve. The data points are pixel positions, which is why the error have to be propagated to the sensitivity value. The pixel errors are estimated by the thickness of the plot line plus an uncertainty of the cursor position and amount to $\sigma_p = 2$ pixel, which corresponds to a maximum sensitivity uncertainty of $\sigma_{S_{rel}}^{max} = 0.01$. The resulting plot is shown in Figure 19. Note that the curve shows the relative sensitivity S_{rel}.

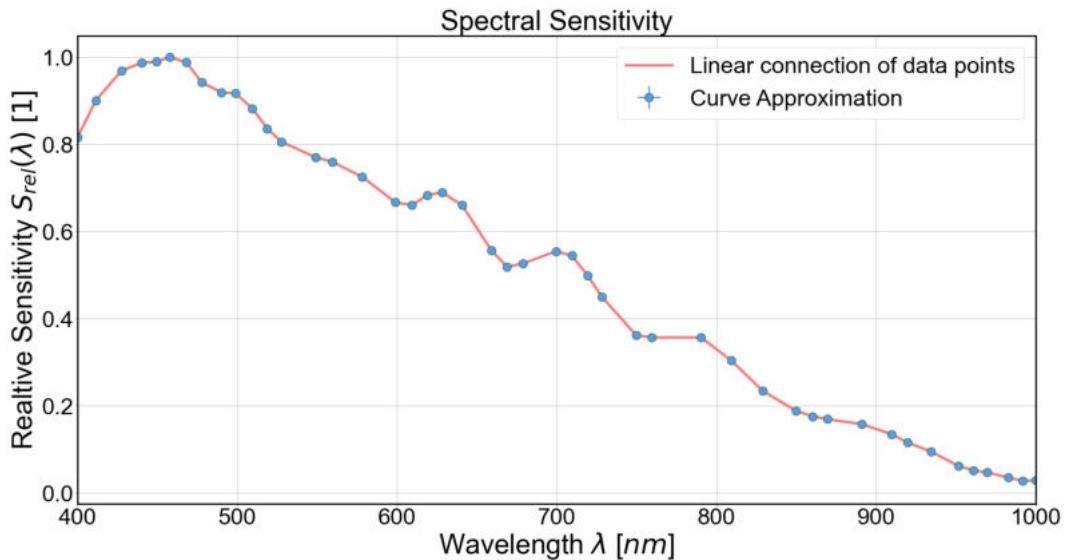Figure 19: Sensitivity curve approximated manually from [26]. The assumed errors are to small to be visible here.

Between the data points of Figure 19, a linear curve is assumed for the sensitivity. If the sensitivity for one value is required, the two nearest points λ_+ and λ_- give a value via a straight line:

$$S_{rel}(\lambda) = \frac{\lambda - \lambda_-}{\lambda_+ - \lambda_-} \cdot (S_+ - S_-) + S_- \ . \tag{4}$$

S_+ and S_- are the corresponding relative sensitivities of λ_+ and λ_-, respectively. To get the actual intensity I, the intensity values I_{raw} have to be multiplied by the sensitivity given at its wavelength:

$$I = I_{raw} \cdot S_{rel} \ . \tag{5}$$

The sensitivity curve is only defined in the range of 400 nm to 1000 nm. Thus, the wavelength range of the spectrometers pixel has to be cut. The range of the spectrometer is approximately from 348 nm to 1028 nm. Additionally, so called "hot" pixel[10] are not being considered. As visible in Figure 22, there are also pixel that do not show the expected behavior. Since this could be an artefact of the LED, it was tested with different LEDs. The spectrum always showed this anomaly, which is the reason why these pixel were also disregarded. This yields 1788 functional pixel in the range of 400 nm to 1000 nm. Pixel that were not considered because there are not functional are visible in Table 6.

Hot pixel	0	344	870	1040	1041	1042	1124
	1128	1141	1426	1427	1550	1907	
Broken pixel	1344	1345	1346	1347			

Table 6: Pixel that were not considered.

There is also an offset on the measurement. It is necessary to prevent negative values of the ADC. A dark current, which occurs due to thermal excitation of charges, also results in an offset. To see if it is dependent on the room temperature and integration time, a dark measurement is done at different temperatures. The spectrometer is heated by a hot air dryer, while the temperature was measured with temperature sensors. For each temperature, 19 different spectra are recorded ranging from an integration time of 50 ms to 950 ms. To get an idea if and how the spectrum changes, the mean value $\bar{I}$ of the whole spectrum is taken. Examples of the temperature dependence of the offset for different integration times is visible in Figure 20. Only the cooldown is considered, since it has less hysteresis.

The non-linearity for temperatures above 30 °C is probably due to a fast temperature change, since the heating is not homogeneous. This results in different values for the temperature sensors and the detector. Therefore, it is a hysteresis effect. Given that the offset depends on both quantities, the room temperature and the integration time, it is reasonable to get the offset for each measured spectrum separately. This is done by considering a part of the spectrum that has no significant light input and taking the mean value of it. Which range of spectrum was taken to take the mean value will be mentioned for each LED.

The dark spectrum also reveals another property of the spectrometer. As visible in Figure 21, the pixel 0 to approximately 600 show a behavior that is not constant. This is why they are not considered for offset determination and corresponds to wavelengths under about 550 nm. The method decreases the amount of intensity values that account for the offset calculation, but due to a remaining range of about 200 nm (550 nm to 750 nm) for an OP130 LED for example, this is not a problem. The standard deviation of the mean value is also a quantity for the noise, which is also integration time and temperature dependent, as shown in Figure 21. When the sensitivity curve and the offset are taken into account, the spectra can be used to take a look at the diodes behavior.

---

[10]Hot pixel are pixel that show unreasonably high intensity values for each measurement. An example is shown in Figure 50 in the appendix.
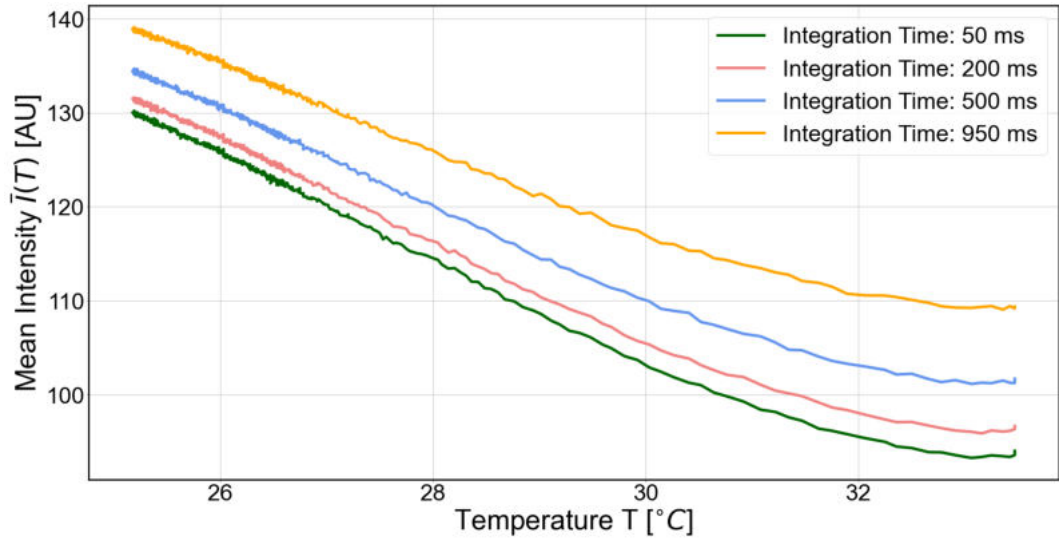
Figure 20: Offset temperature dependence for different integration times. The non-linearity for high temperatures is probably due to a fast change of T, due to heating. It causes a difference between the temperature of the spectrometers detector and the temperature sensor on top.
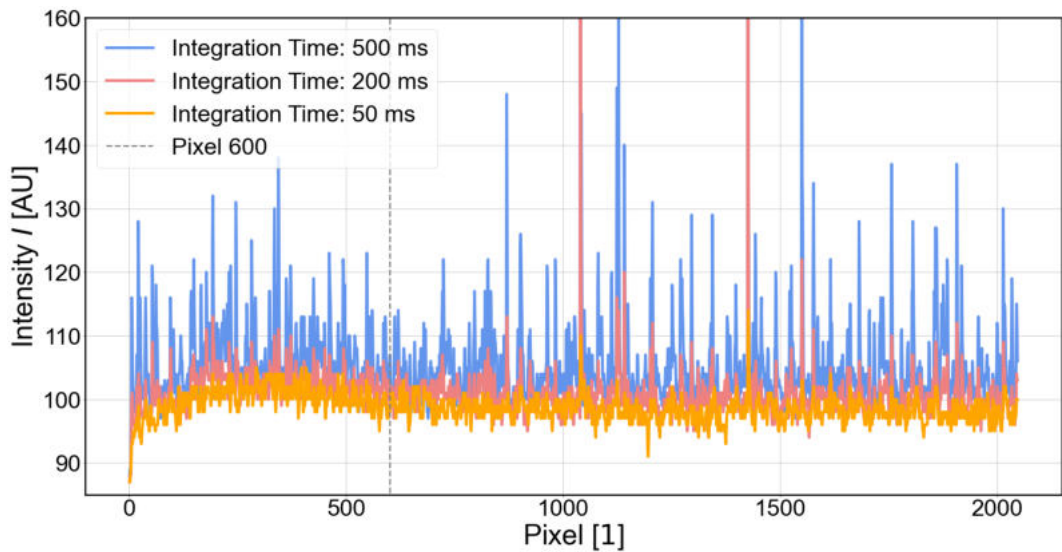

Figure 21: Example of an offset measurement with no light input in the spectrometer. These spectra were recorded at a room temperature of $32.8\,^{\circ}$C. Note that they are raw spectra, which is why all pixel are visible.

3.2   OP130

The OP130 from TT Electronics is a gallium arsenide (GaAs) diode with a wavelength of 935 nm [13]. To measure its spectrum, an integration time of 3 ms is chosen. This is the minimum integration time of the spectrometer and used, because the optical fiber inside the vacuum chamber has a thickness of 600 μm, which is larger than the 400 μm thick fiber used for the other LEDs. To prevent the spectrometer from saturating, a reduction tube with a length of 2 cm is used.
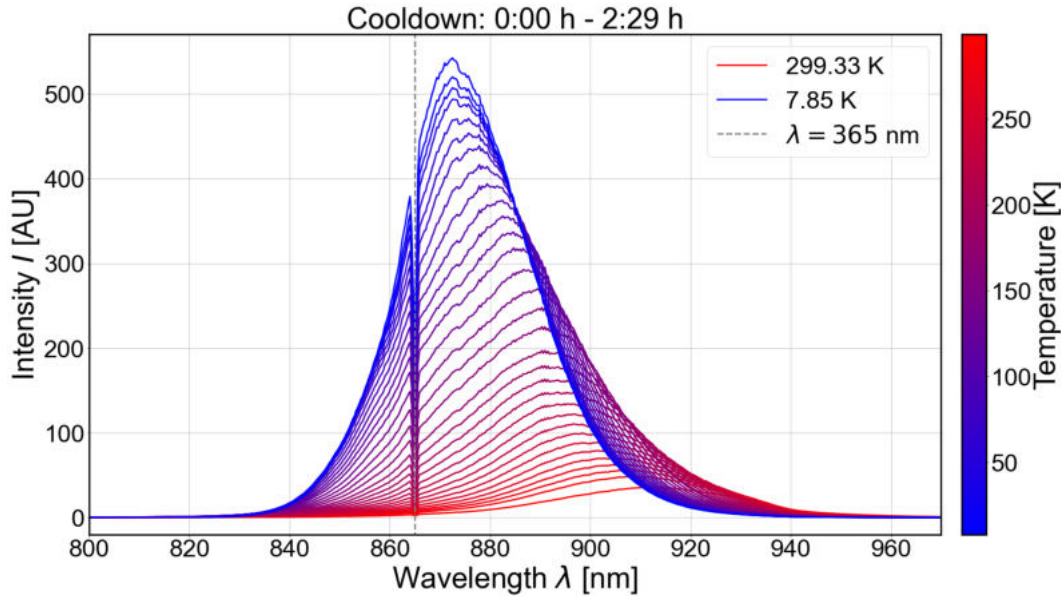

Figure 22: OP130: Measured spectra dependent on the temperature for the cooldown. The temperature dependency is visualised via the color of each spectrum.

Figure 22 shows the behavior of the LEDs spectrum dependent on the temperature. This plot is obtained when taking only spectra that have a temperature difference of at least $\Delta T = 7.5$ K between them. The first thing that stands out is the sudden intensity reduction at around 865 nm. Since this is an artefact that occurs for all LEDs, these pixel will be neglected from now on. The spectrometer does not seem to work in this range. The associated pixel are pixel 1499 to 1502. The resulting plot is visible in Figure 23 (a). The corresponding plot for the warm-up can be found in Figure 23 (b). It shows that the wavelength decreases with lower temperature, while the intensity increases significantly. Such a spectrum has different properties that will be considered. The important quantities here are the peak position, the peak width and its height and how they behave with changing temperatures.

Notice that the LED does not emit light with a wavelength of 935 nm at room temperature. It is about 912 nm. A reason for that difference might be a manufacturing error, although the discrepancy is probably too large for that to be the case. The full width at half maximum (FWHM) of the peak is 50 nm at a current of 10 mA, according to the data sheet [13]. This is probably still not enough to explain this behavior, since 935 nm − 912 nm = 23 nm is almost more half of the FWHM

(25 nm). Another possible explanation would be a wrong calibration of the spectrometer, but since the other tested LEDs show no signs of that, even at the similar wavelength, this is most likely also not true. Additionally, the largest data point used for calibration is also at 912 nm. The cleaning process in an ultrasonic bath could be a reason. If the LED is not sufficiently sealed, as stated in [13], the water and isopropanol used during cleaning might change the LEDs properties. Either way, the LED will be analysed regardless of this wavelength difference.
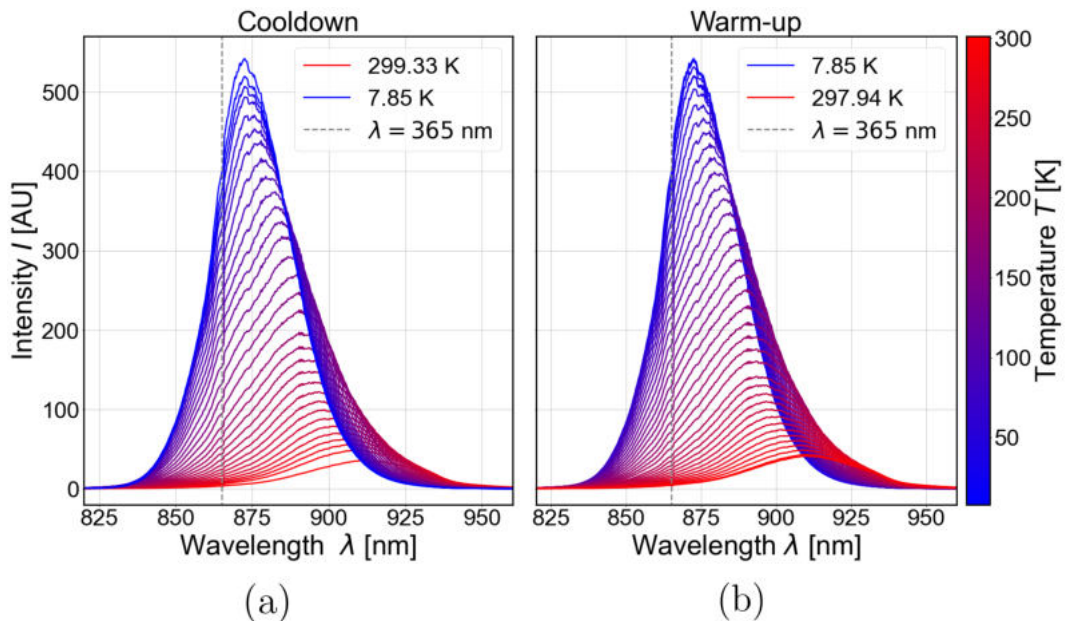

Figure 23: OP130: Measured spectra dependent on the temperature for the cooldown (a) and the warm-up (b) without the intensity artefact at around 865 nm. The temperature dependency is visualised via the color of each spectrum.

To get the position of the peak wavelength, each spectrum peak is approximated by a parabola $I(\lambda) = a(\lambda - b)^2 + c$. Even though the peak is not perfectly symmetrical, it is sufficient to be approximated via a parabola. The reason for a parabola is the approximation of a gaussian distribution at its peak. The statistical input errors $\sigma_{I,stat}$ and $\sigma_{\lambda,stat}$ are taken from the calibration of the spectrometers intensity and wavelength. An example of such a peak approximation is shown in Figure 24 (a).

The lower fit boundary is calculated by considering the maximum intensity wavelength λ_{max} and taking the wavelength that is 15 indices lower, which is $\lambda_{low} = 879.74$ nm for this peak. The upper limit is determined by adding 20 indices: $\lambda_{up} = 890.94$ nm. This asymmetrical fit is chosen, because it yields the best result for the fit parameters. This is due to the asymmetrical shape of the spectrum. Since the errors shown in Figure 24 (a) are large, the $\chi^2/N_{dof} = 0.034$ is very small. Nevertheless, the resulting fit parameters are reasonable, so it is concluded that the peak values are determined well. The parameters of the shown fit are visible in Table 7. Here, b is the peak position and c the corresponding peak intensity. a describes the slope of the fit and is therefore not a factor that is discussed further.
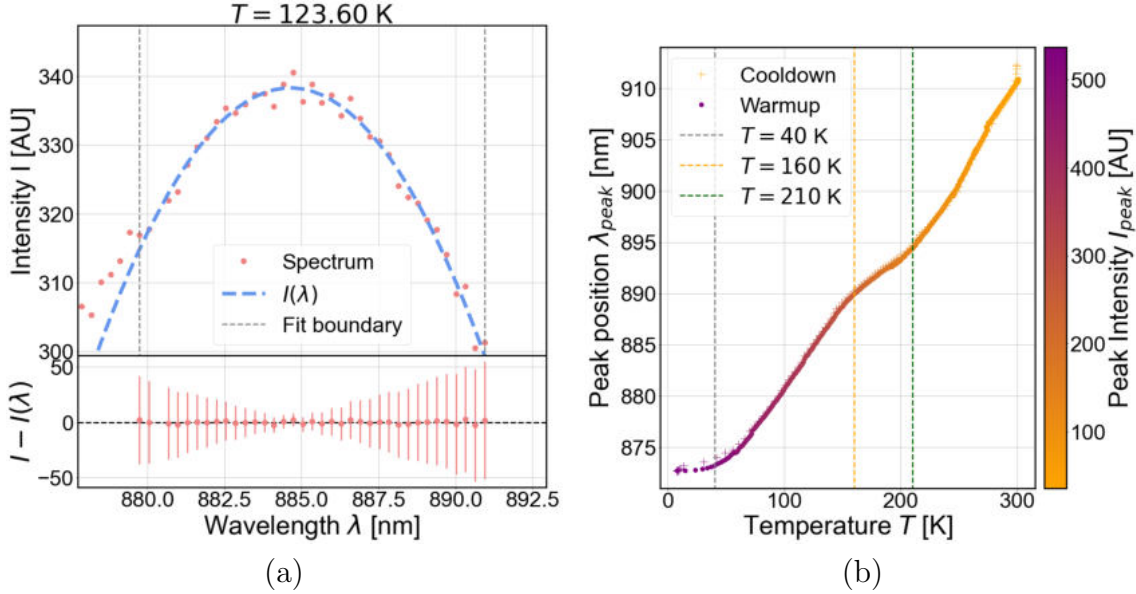
Figure 24: OP130: (a) Example of a quadratic peak fit $I(\lambda) = a(\lambda - b)^2 + c$ at $T = 123.60$ K. $\chi^2/N_{dof} = 0.034$. (b) Peak positions as a function of temperature. The peak intensity is shown as the point color.

The peak determination is done for all spectra of one cooldown cycle, including the warm-up.

The peak position dependent on the temperature can be seen in Figure 24 (b). The difference between the maximum and minimum wavelength is 39.58 nm. Its intensity rises by a factor of approximately 15 from $I_{peak}^{min} = 35.5 \pm 0.3$ to $I_{peak}^{max} = 537 \pm 3$. At high temperatures over 210 K, the peak position decreases almost linearly. The decrease becomes less between 210 K and 160 K and rises to a similar value from 160 K to 40 K as it has over 210 K. Under 40 K the peak position does not change a lot and becomes almost constant for low temperatures under 30 K. Since this behavior is visible for cooldown and warm-up, it is unlikely that the peak determination itself accounts for these effects. An important factor is the temperature dependence of the energy band gap E_g. If it increases in value, the energy of electron transitions increases as well and therefore the emitted photon wavelength becomes smaller. The shape of $E_g(T)$ is shown in Figure 51 in the appendix. It also has the linear temperature dependence for approximately $T > 40$ K and gets almost constant for lower temperatures. Since the behavior of the band gap energy and the peak position are that similar, it is concluded that the main effect for the LEDs peak position behavior is caused by this energy dependence on the temperature. Other effects like the charge carrier mobility might also have an effect on this behavior, but it is not visible enough in Figure 24 (b).

$a \pm \sigma_{a,stat}$	$b \pm \sigma_{b,stat}$	$c \pm \sigma_{c,stat}$	χ^2/N_{dof}
-0.9 ± 0.2	884.6 ± 0.3	338 ± 2	0.034

Table 7: Fit parameters for the peak shown in Figure 24 (a).

To determine the power output of the LED, it is necessary to integrate over the

spectrum. Since the peaks are asymmetrical, an analytical approach via a guassian curve is not possible. For this reason, the power is calculated by summing over the intensities in a certain range of the spectrum that includes the peak. The partial summation yields better results due to the irregularities in the offset (see Figure 21). The chosen part for the OP130 spectrum ranges from 800 nm to 980 nm. Because an absolute value of the power cannot be calculated as a result of the arbitrary unit of the intensity, it is presented in reference to the initial value P_0 at time $t = 0$ s. This power will be called the normalized power $P_{norm}(T) = P(T)/P_0$. The normalized power displays the increase of power compared to the power output at room temperature. The plot is shown in Figure 25 (a). It rises monotonically by approximately 865%. The slope decreases under 120 K and gets almost to zero at the lowest temperatures, so there is no significant change in power output of the diode under 20 K. This constant behavior is consistent with the nearly constant peak position at low temperatures shown in Figure 24 (b). Therefore, the LED has a stable optical behavior at this temperature range. Between 120 K and 200 K, a linear relation between temperature and optical output power is measured. For higher temperatures than 200 K, the power decreases. It might even out at a constant value near zero for higher temperatures, which is not testable here. Since the output power is closely related to the peak width and its height, their behavior will be shown too. This way, it is possible to distinguish between a power increase because of a wider peak or a larger peak intensity.
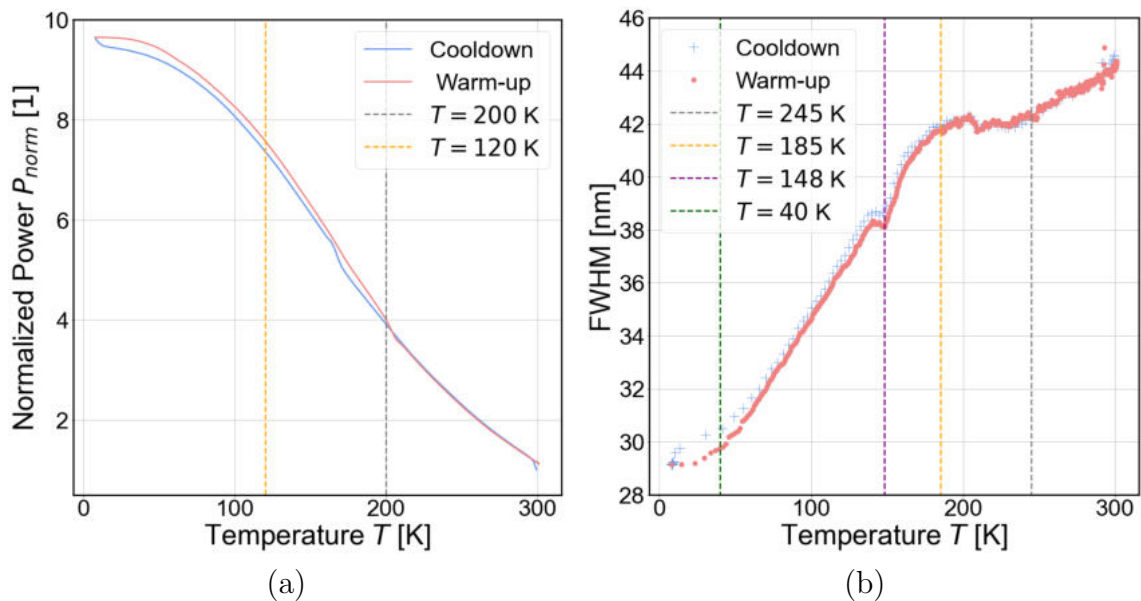

(a)   (b)

Figure 25: (a) Peak output of the diode with respect to the starting value P_0 depending on the temperature. (b) Temperature dependence of the FWHM.

The peak width can neither be determined via a gaussian fit due to the asymmetrical spectrum shape. This is why the FWHM is taken as a quantity of peak width. Since half the maximum does not have an exact data point on the left and right hand side of the peak, a linear approximation between the two nearest points was done. The equation used is analogous to Equation 4. The peak widths dependence on the temperature is shown in Figure 25 (b). The width of the peak gets smaller with lower temperatures. It decreases almost by a third from 44 nm at room

temperature to under $30\,\text{nm}$ at $7.85\,\text{K}$. Above $T = 220\,\text{K}$, the peak width changes linearly. It is reduced by approximately $2\,\text{nm}$ over a temperature range of $80\,\text{K}$, which corresponds to $\Delta\lambda_{FWHM}/\Delta T = 25\,\text{pm/K}$. This behavior is very similar to the power at these temperatures (see Figure 24 (a)). For $185\,\text{K} < T < 245\,\text{K}$, the width stays almost constant at $42\,\text{nm}$. Between $185\,\text{K}$ and $40\,\text{K}$, the peak width decreases almost linearly with the lowering temperature. The only exception is at $T = 148\,\text{K}$, where the peak width dips. Under $40\,\text{K}$, the width decrease becomes less and is almost constant at the lowest measured temperatures. Except for the dip, the behavior can explain the low temperature part of the power plot. The slope decreases due to the decreasing peak width. Since the peak width is related to the state density, this seems to be the underlying temperature dependence of the power output at low temperatures.

The peak intensity shows a very similar temperature dependence as the optical power, as shown in Figure 26 (a). This suggests that the influence on the power of the peak height is stronger than the influence of the peak width. The peak intensity curve has an almost linear part between $60\,\text{K}$ and $205\,\text{K}$. At temperatures below $60\,\text{K}$, the hysteresis gets stronger and a less step temperature dependence is measured. Above $T = 205\,\text{K}$, the dependency is also nearly linear, but with a different slope than between $60\,\text{K}$ and $205\,\text{K}$. Since the peak intensity is basically a measurement of the number of photons at the peak wavelength, there could be multiple reasons for this behavior. The transparency of the semiconductor could get better resulting in more photons that are able to escape. Another reason would be a higher number of charge carriers inside the material that can emit photons.

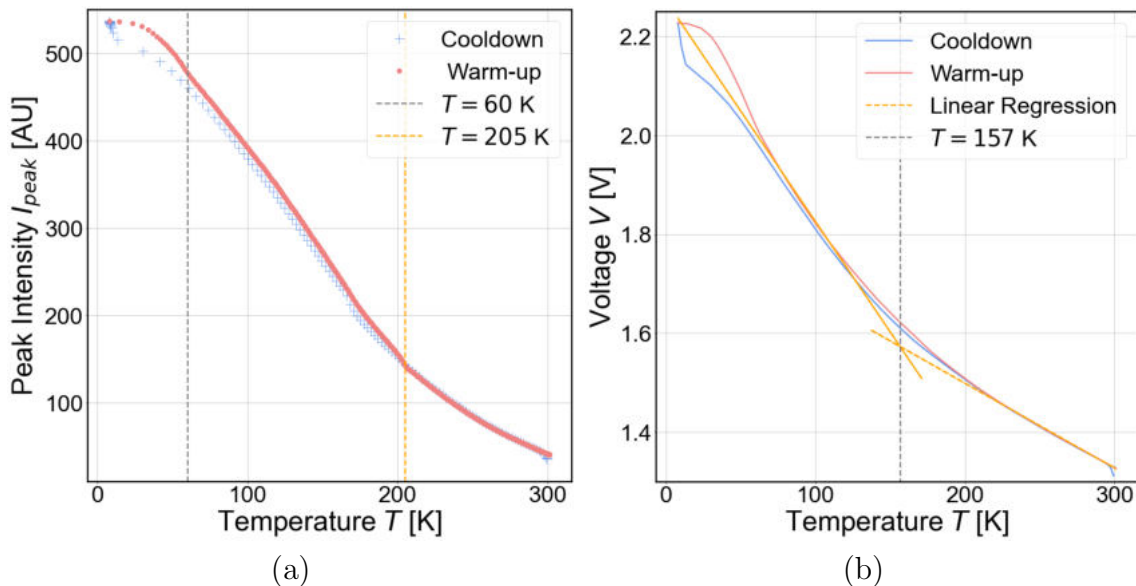| (a) | (b) |

Figure 26: OP130: (a) Temperature dependence of the peak intensity. The cooldown and warm-up is shown separately. (b) Forward voltage as a function of temperature split into cooldown and warm-up. Two linear regression are shown as orange lines, with their intersection at $T = 157\,\text{K}$. The displayed temperature sensor is fixed onto the LED mounting.

The measured forward voltage V dependent on the temperature is shown in Figure 26 (b). The hysteresis effect occurs, because the LED is cooled later than

the temperature sensor next to it. For sufficiently large temperature changes, an inaccurate mapping of the actual temperature of the LED and its forward voltage follows. The actual forward voltage at low temperatures lies in between the cooldown and warm-up measurements. The forward voltage increases by 915 mV, which corresponds to a factor of approximately 1.7 compared to the voltage at room temperature. The curve can be divided into two parts shown by the gray line at $T = 157$ K, which both show a linear temperature dependence. Remember that the real forward voltage lies between the red and blue lines. The linear regression was made for values under 120 K and over 210 K. This behavior was also seen in [27] by other gallium based LEDs (see Figure 52 in the appendix). The linear regression yield $dV/dT = -1.4$ mK/V for higher temperatures and $dV/dT = -4.5$ mK/V for low temperatures. According to [27], there are three main components that lead to this temperature dependence: the intrinsic carrier concentration, the band gap energy and the state density in the valence and conduction band. The latter gives a lower boundary for the temperature dependence, so it is relevant at high temperatures. It is a description of the number of modes per frequency range. This means that a high state density corresponds to a lot of possible different electron transitions in a small range of energy. This is why the state density is closely related to the peak width for a given optical power. For lower temperatures, the intrinsic carrier concentration is dominant. It describes how many charge carriers like electrons or holes can be found within a certain volume. It is a measure for the amount of photons that can be emitted by the semiconductor and can thus be characterised via the peak intensity. The energy band gap gives an additional temperature dependence, as seen in Figure 51. Keep in mind that there are other factors that are not considered here, like the resistance of the LED, which also depends on the temperature.
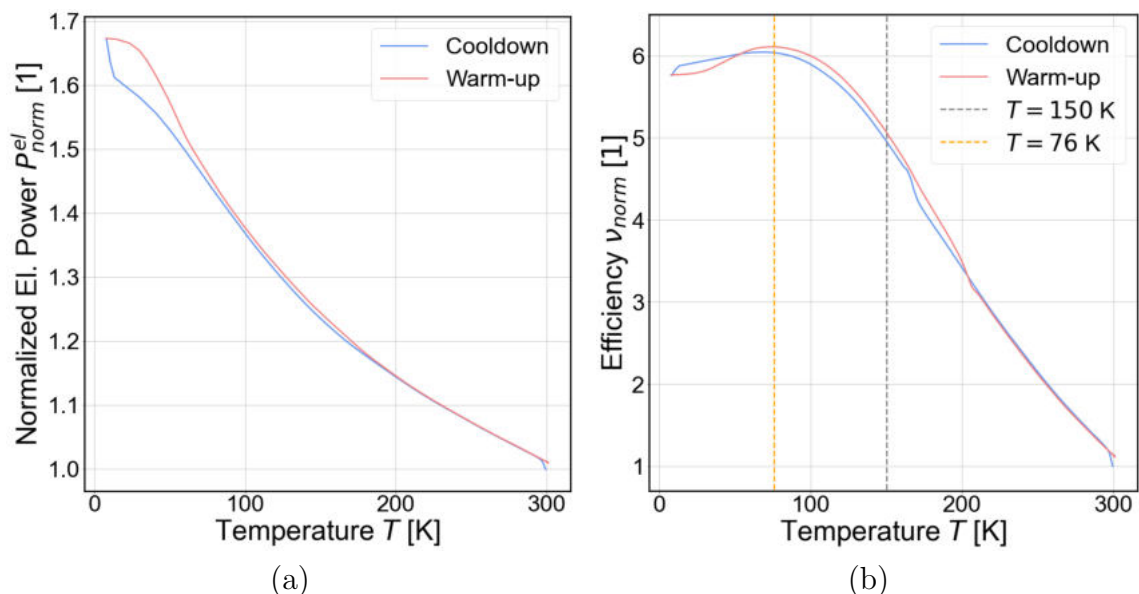

Figure 27: OP130: (a) Normalized electrical input power as a function of temperature. (b) Normalized efficiency $\nu_{norm} = \nu/\nu_0$.

The question now is whether the efficiency of the LED actually increases with the power output. Since the forward voltage also increases (see Figure 26 (b)) with

lower temperatures, a rise in efficiency cannot be inferred from this. The electrical input power can be calculated via $P_{el} = V \cdot I$. The current values I are determined with the ADC board calibration explained in section 2. As done with the optical power, the normalized electrical power P^{el}_{norm} is given by dividing by its starting value P^0_{el}. The resulting plot is shown in Figure 27 (a). It is not surprising that the curve looks very similar to the forward voltage in Figure 26 (b), since the current does not vary by a lot and is therefore nearly a constant factor.

The efficiency ν is the ratio between input and output power: $\nu = P/P_{el}$. The results are normalized through the starting efficiency value via $\nu_{norm} = \nu/\nu_0$ to get a reference point, as it was done for the power. The plot is shown in Figure 27 (b). For temperatures between $300\,\text{K}$ and $150\,\text{K}$ the increase in efficiency is nearly linear. As the individual quantities behave monotonously, it is unexpected to see the efficiency peaking at $76\,\text{K}$. The highest efficiency is 6.11 times the minimum. It decreases to 5.8 times the minimum at $T = 7.85\,\text{K}$. At temperatures above $150\,\text{K}$, ν_{norm} increases almost linearly with lowering T. This means that the output power rises by a constant factor more than the electrical input power.
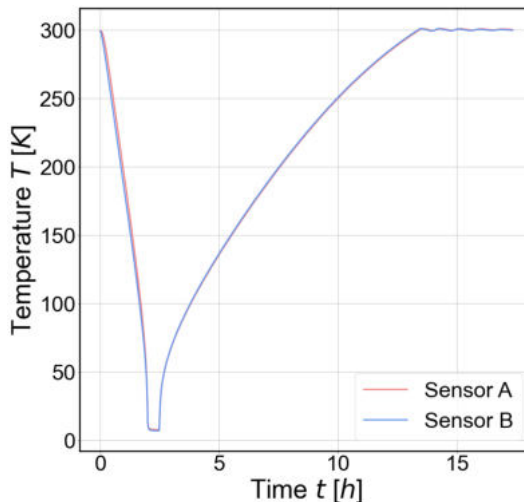

Figure 28: OP130: Temperature progression with time. Sensor A is the temperature detector in the LED mounting and Sensor B sits under the cooling plate. This is a typical temperature curve for a cooling cycle.

It is not clear so far if the shown effects on the LED occur for all cooling cycles or changes each time. This is tested by doing multiple cycles with the same LED. There are a few differences that will be mentioned. Things that do not change are not be elaborated further. In Figure 29 (a), the voltage of two example cycles are visible. Cycle 1 is the run that was discussed above. The starting value of the voltage at room temperature is the same, as expected. The shape of the the curve stays the same too, only the maximum voltage is different and the curve is stretched as a result. Since the time development is qualitatively the same, the discussion above is still valid.

For the optical power output this pattern is the same, as seen in Figure 29 (b). In cycle 2, it rises not by 865% as in cycle 1, but by 639%. The effect on the voltage gets even more apparent when factoring in the corresponding current. This yields the normalized electrical input power shown in Figure 29 (c). The room temperature values of the input and output power are also not the same. As a result of these two quantities, the efficiency shows a significant difference between the cycles too (see Figure 29 (d)). As said before the qualitative discussion stays the same, but with different values. The reason for the different output power is probably the LED mounting, which does not fix the diode in a stable position. Since the cryostat vibrates during operation, the LED could change position. Asymmetries in the light profile could then cause changes of the output power and its measurement. Still,
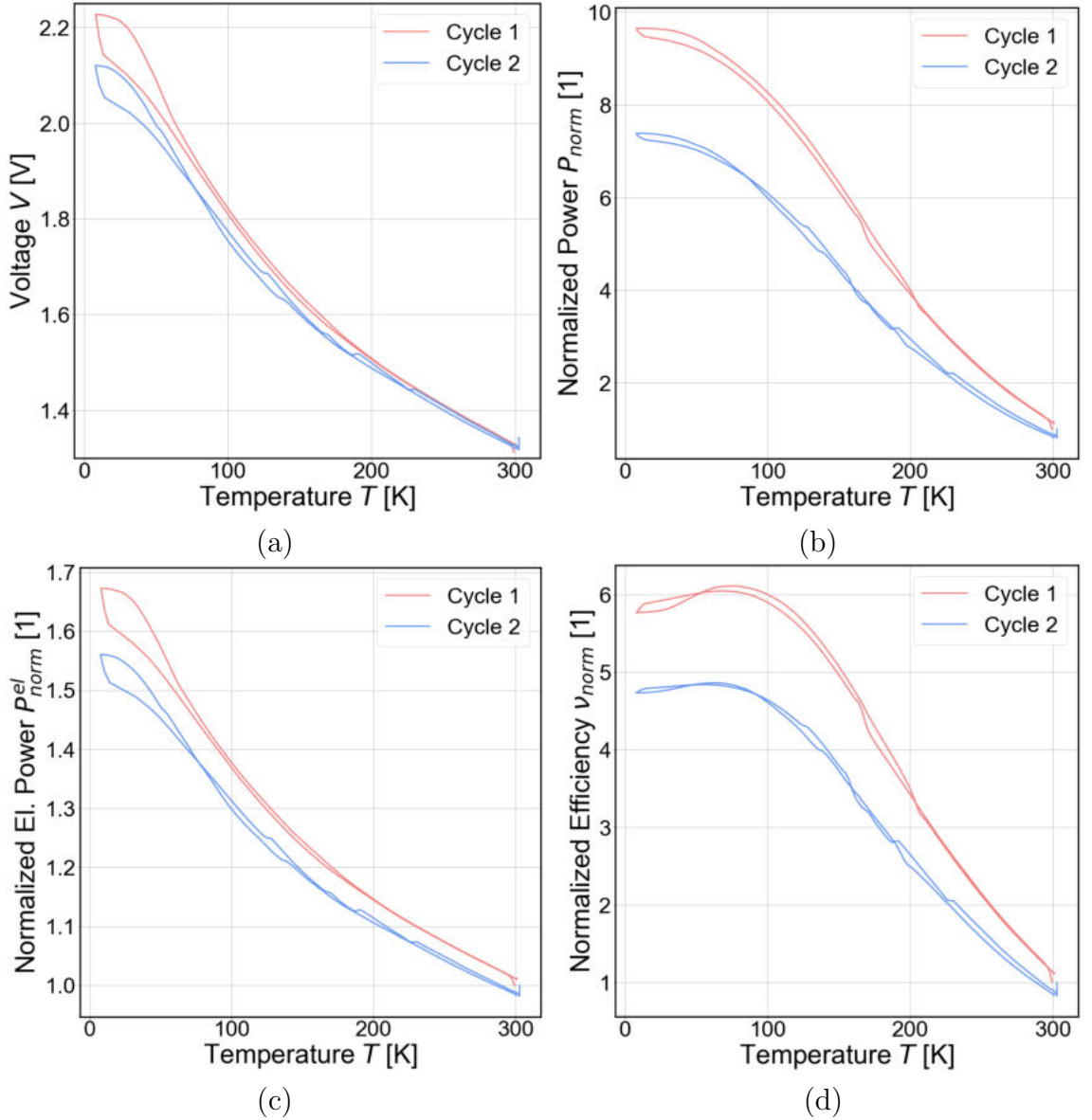
Figure 29: OP130: Comparison of two cooling cycles for (a) the forward voltage, (b) the output power, (c) the electrical input power and (d) the efficiency of the diode.

this is not an explanation for the different forward voltage values. This is why it is concluded, that the LED shows a non-stable behavior at room temperature, but even more so at cryogenic temperatures.

Since the peak position cannot be determined for all LEDs, it is necessary to get a different kind of peak calculation. This is due to very asymmetrical spectra for other LEDs. To get a usable quantity of the peak position, a weighted peak is determined:

$$\lambda_{peak}^{w} = \frac{\sum\limits_{i=0}^{N} \lambda_i I_i}{\sum\limits_{i=0}^{N} I_i} \ . \tag{6}$$

I_i is the corresponding intensity value for each wavelength λ_i. If the spectrum was a physical object, λ_{peak}^w would be the centre of gravity. This does not give the exact peak value, but a good evaluation of how the spectrum behaves. As seen in Figure 30 (a), the behavior is very similar to the actual peak position with the decrease for temperatures above $50\,\mathrm{K}$ and becomes almost constant below. To get a parameter of the peak width, the statistical uncertainty of the weighted peak is taken. The normalized result is shown in Figure 30 (b). Since the behavior of this error is not similar to the peak width of the LED in Figure 25 (b), this is not a good variable for the peak width and will not be discussed any further.
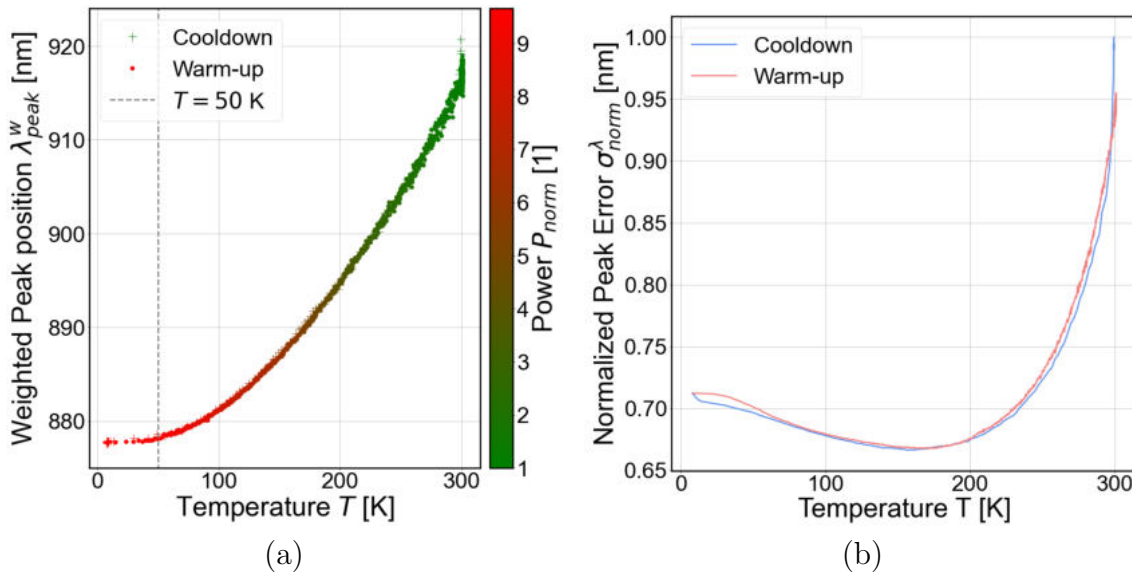
Figure 30: OP130: (a) Weighted peak positions as a function of temperature. (b) Normalized error of the weighted peak position.

3.3   OP232

The OP232 from TT Electronics is a LED that emits light with a wavelength of 890 nm. It is made of gallium aluminium arsenide (GaAlAs) [28]. An integration time of 30 ms is chosen with 45 s between each measurement. The recorded quantities are the same as for the OP130 LED. Since the results are not reproducible with the setup used for this the OP130, a new LED mounting is used for the OP232. This mounting holds the LED in position by pressing the copper lid on it (see Figure 10 (a)), so that it cannot move. The fiber inside the vacuum chamber is also changed to a 200 µm thick fiber. The reduction tube and the fibers outside the vacuum chamber stay the same.
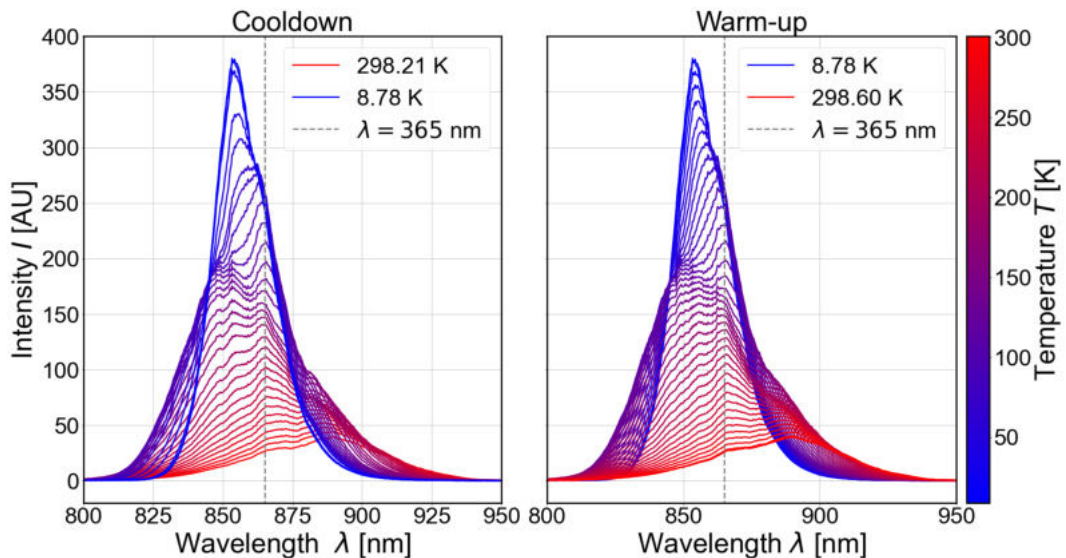
Figure 31: OP232: Temperature dependence of spectra for the cooldown (left) and the warm-up (right) without the intensity artefact at around 865 nm. The temperature dependency is visualised via the color of each spectrum.

The measured spectra are shown in Figure 31. They have a very asymmetrical shape, especially for lower temperatures under 200 K. The jump in intensity at $\lambda = 865$ nm is the result of cutting out the abnormal behaving pixel from Figure 22. It looks like the peak wavelength gets smaller and increases again. To see if this is true, the peak needs to be determined. As explained before, a parabolic peak approximation is not possible due to a strong asymmetry of the peak. As visible in Figure 31, the spectrum has two peaks at temperatures between 100 K and 200 K. Therefore the weighted peak is calculated via Equation 6. The result is shown in Figure 32 (a). As discussed before, the weighted peak is only a qualitative description of the peak position. This is why the actual peak positions might vary from them. For temperatures above 180 K, the peak decreases linearly with decreasing temperature. To evaluate this behavior, it is necessary to take a look at other gallium based semiconductors. For example, the gallium phosphide (GaP) shows nearly the same qualitative band gap temperature dependence [29]. For this reason, it is assumed that gallium base LED behave in this particular way (see Figure 51 in the appendix). A similar effect on the peak position was seen by the OP130 LED too,

so it is likely that the energy band gap dependency on temperature is responsible for this effect. At $T = 99\,\text{K}$, the weighted peak reaches its minimum value of $857\,\text{nm}$. Below this temperature, λ^w_{norm} increases to reach a constant value of approximately $859\,\text{nm}$ for temperatures under $40\,\text{K}$. As expected from the spectra in Figure 31, the weighted peak rises for very low temperatures to reach a stable value. This behavior cannot be explained by the temperature dependence of the energy band gap, assuming its behavior is similar to other gallium based semiconductors. Different energy occupation might be the cause. When lowering the LED temperature, the dominant energy transitions change, which could result in a increase of energy for the average photon.
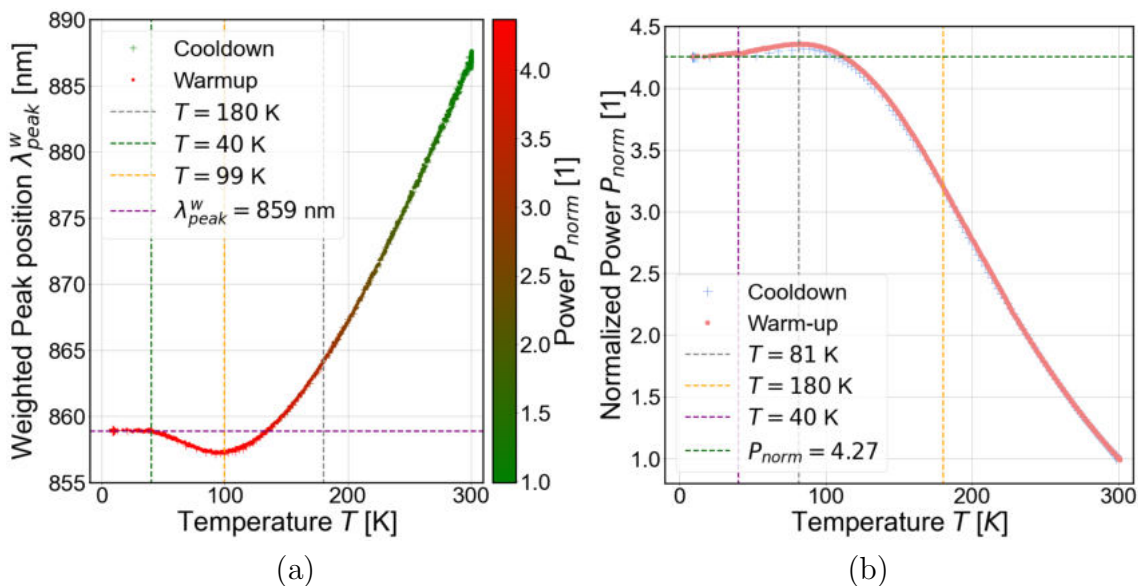
Figure 32: OP232: (a) Weighted peak positions as a function of temperature. The normalized power is described by the color of each point. (b) Normalized power output of the diode as a function of temperature.

As before, the power is the sum of the intensity values at a certain range. The chosen range for the OP232 is $780\,\text{nm}$ to $960\,\text{nm}$. The power was again normalized by dividing by the starting value at room temperature to get a reference point. Its temperature dependence is shown in Figure 32 (b). The progress also shows a simple nearly linear temperature dependence for $T > 180\,\text{K}$. At $81\,\text{K}$, the power reaches a maximum that is 4.4 times larger than its starting value. The optical power then decreases to a constant value of about 4.27 times the power at room temperature. The power curve behaves similar to the weighted peak position. There is a maximum (or minimum) value and a nearly constant result at temperatures under $40\,\text{K}$. A difference is the temperature at which the maximum and minimum values are reached. For low temperatures under $180\,\text{K}$, the transparency of the semiconductor may have an impact on its power output. If the photons that are emitted by electron transitions in the material get absorbed by the semiconductor itself, less light and therefore less power is able to escape. This could explain the decrease of power for $T < 81\,\text{K}$.

Whether the power rises due to an increased peak width or an increased intensity itself can be determined by plotting the FWHM. Because an actual peak intensity
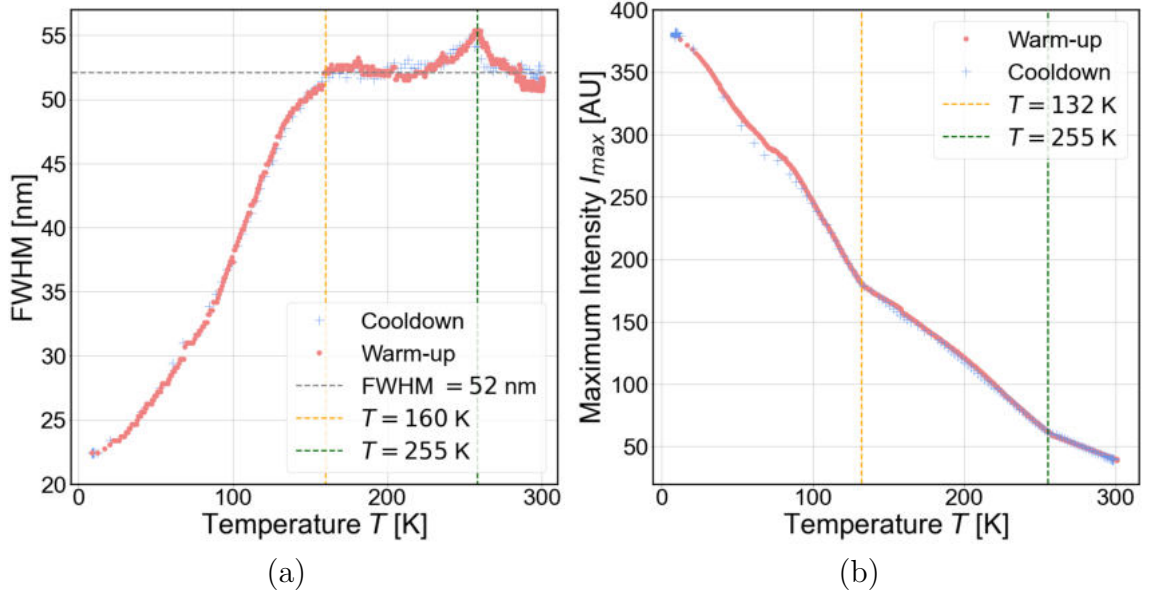
Figure 33: OP232: (a) FWHM with respect to the maximum intensity of each spectrum. (b) Temperature dependence of the maximum intensity value.

cannot be determined, the maximum value of each spectrum is taken. This should yield a good result since the switch between two maxima in a spectrum with more than one peak does not effect the curve of the maximal intensity. The result can be seen in Figure 33 (a). The constant peak width for temperatures above 160 K of approximately 52 nm is interrupted by a peak at $T = 255$ K. Since this peak happens for both, cooldown and warm-up, it is more likely to be a spectral effect rather than a calculation error. It is possible that the peak is a result of a broader range of transitions that the electrons are able to use for photon emission. For temperatures above 255 K, this would mean a certain dominant photon energy and a different one for temperatures below 255 K. For a given constant power this would mean a smaller state density. The peak would then describe the crossover of two dominant energy transitions. For $T < 160$ K, the FWHM decreases rapidly and reaches a minimum at the lowest measured temperature of 8.78 K. The corresponding peak width is $\lambda_{FWHM}^{min} = 22.5$ nm. It can be concluded that the peak width is not accountable for any significant power gain above $T = 160$ K, but for the power decrease below this temperature.

The maximum intensity, as shown in Figure 33 (b), increases monotonously with decreasing temperature. At $T = 255$ K, the slope gets more steep, which is also the case for $T = 132$ K. Considering the FWHM, it is reasonable to assume that the behavior of the maximum intensity is the reason for the power increase at temperatures above 160 K. Physically, the increasing maximum intensity describes an increase of number of photons at a specific wavelength hitting the detector. This means an increase in power too and is connected to a larger charge carrier density. Apparently, the width decrease at $T < 160$ K is has a larger influence on the power output than this increase in maximum intensity.

The measured forward voltage is shown in Figure 34 (a). The temperature dependence is very similar to the forward voltage of the OP130. At room temperature, the diode has a forward voltage of approximately 1.32 V. The maximum voltage value at

$T = 8.78\,\text{K}$ equals $3.09\,\text{V}$. The linear regressions for low and high temperatures can be done in the same way as for the OP130, but at different temperature ranges. The regression for lower temperatures was done for $T < 50\,\text{K}$ and for higher temperatures at $T > 200\,\text{K}$. This yields a temperature dependency of $dV/dT = -19.9\,\text{mK/V}$ for low temperature and $dV/dT = -1.6\,\text{mK/V}$ for higher temperatures. As explained before, the main reason for the voltage increase at high temperatures are changes in the state density of the valence and conduction band. For lower temperatures, the dominant factor is the intrinsic carrier concentration [27]. This behavior seems to be valid for different gallium based diodes, as the OP130 and the OP232 show a similar curve.
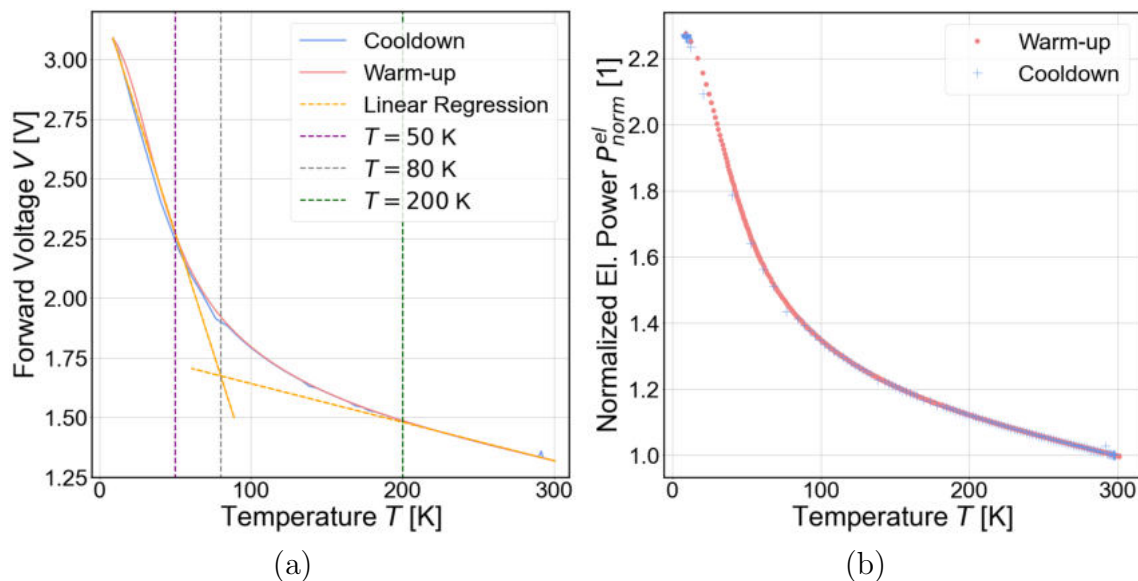
Figure 34: OP232: (a) Forward voltage as a function of temperature. The linear regressions are shown to make the linear behavior in different temperature ranges visible. (b) Temperature dependency of the normalized electrical input power.

To get the temperature dependency of the efficiency, the electrical input power needs to be determined. As for the OP130 LED, this is done by using $P_{el} = V \cdot I$, where the current I is determined via the calibration described in section 2. The normalized electrical power is visible in Figure 34 (b). It is again not surprising that it has the same shape as the forward voltage due to the nearly constant current supplied by the LED driver board. Over a range of $292\,\text{K}$, the input power rises to a maximum of 2.27 times its value at room temperature.

The efficiency $\nu = P/P_{el}$ is shown in Figure 35 (a). It is normalized as it was done before. For temperatures $T > 180\,\text{K}$, the efficiency rises almost linearly up to 2.78 times its starting value. Then, the slope decreases and reaches a maximum efficiency at $T_{max} = 119\,\text{K}$. The corresponding efficiency ν_{max} is 3.27 times the efficiency at room temperature. Below T_{max}, the efficiency decreases with approximately the same slope magnitude as it increased before. At temperatures lower than $60\,\text{K}$, the change is nearly linear again until the coldest temperature of $7.78\,\text{K}$ is reached with an efficiency of $\nu_{norm} = 1.87$. This large decrease for low temperatures is the result of the steep increase in electrical input power, as visible in Figure 34 (b). During this time, the output power remains almost constant or even decreases (see Figure 32

(b)). For low temperatures under 80 K, this yields a dominant factor for the behavior of the LED, which is the state density. The change of electrical input power is most relevant, which is a result of the increasing forward voltage and therefore the state density as stated in [27]. At higher temperatures above 160 K, the output power is the dominant factor, which changes due to the changing maximum intensity. This is related to the number of photons that the semiconductor emits. There could be multiple reason for this, e.g. the transparency of the material or the charge carrier concentration. Since the output power is an important variable for the use of an OSEM, it is concluded that the behavior at temperatures under 40 K is quite stable, as shown in Figure 32 (b).

(a)   (b)
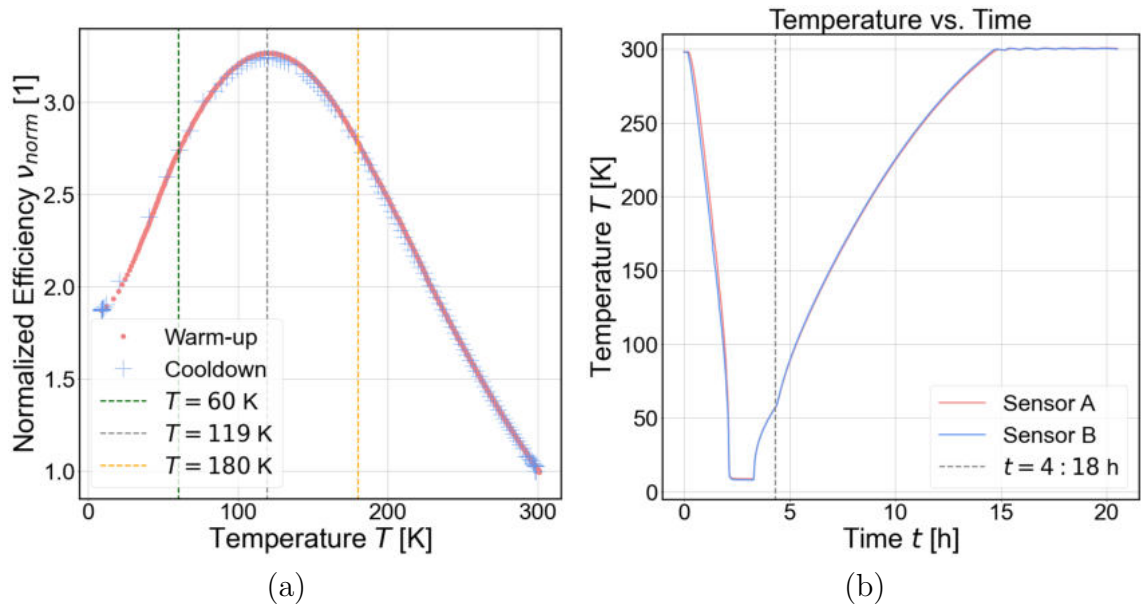
Figure 35: OP232: (a) Temperature dependence of normalized efficiency. (b) Temperature as a function of time. The start of heating can be seen at $t = 4:18$ h.
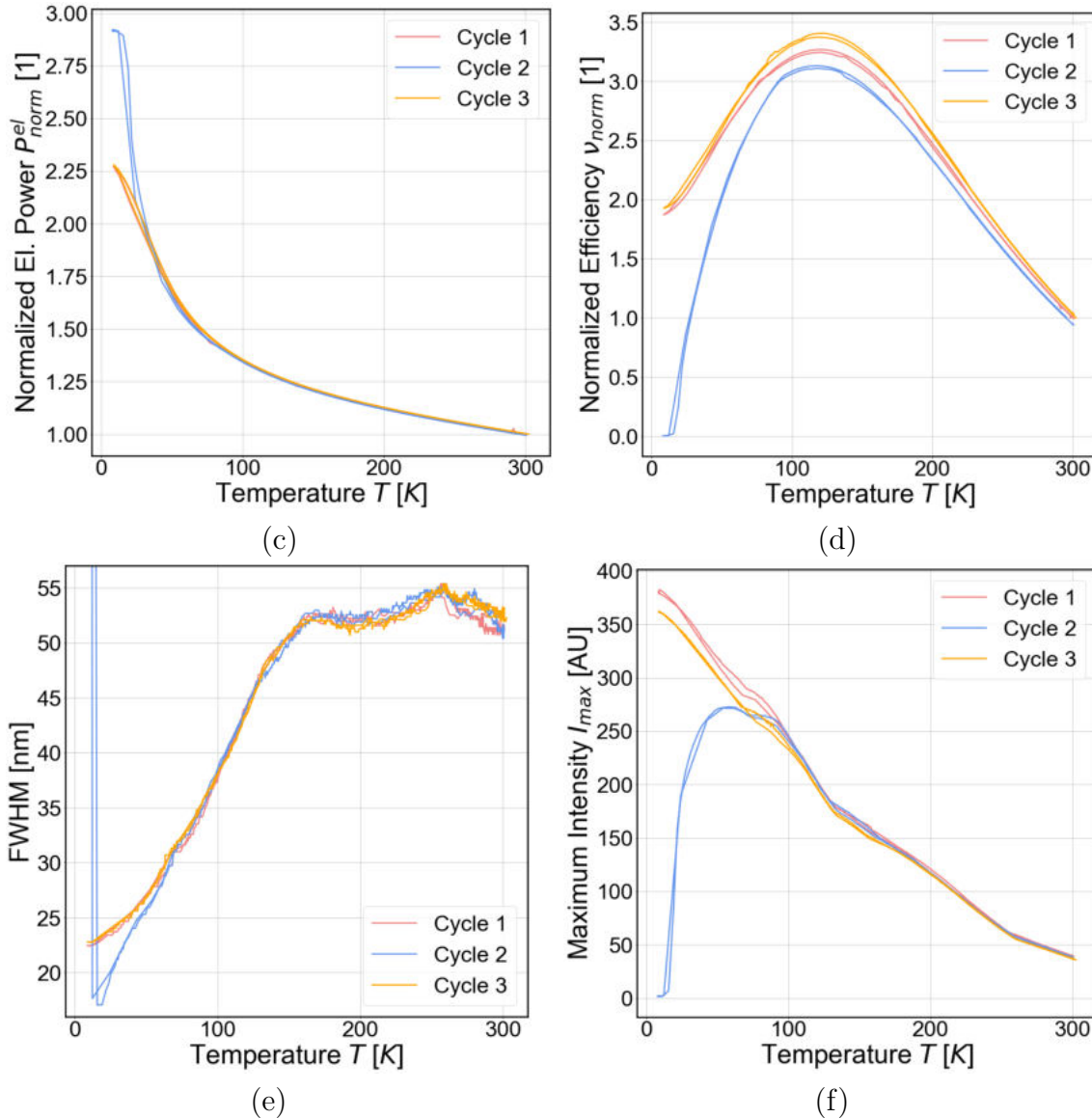

(a)   (b)
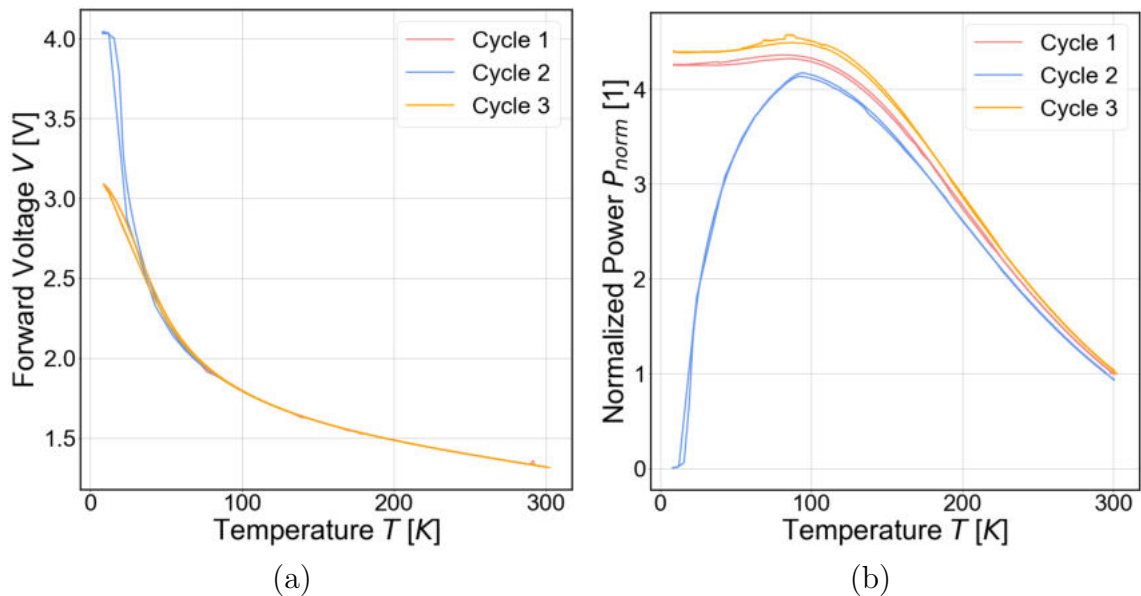
Figure 36: OP232: Comparison of three different cooling cycles of (a) the forward voltage, (b) the opitcal power output, (c) the electrical input power, (d) the efficiency of the diode, (e) the FWHM and (f) the maximum intensity.

Another thing that should be mentioned, is the start of the heating phase during warm-up. This can be seen in Figure 35 (b). The buckling at $t = 4 : 18$ h is the result of the heating turning on. Its temperature to be reached is 300 K.

To verify the analysis above, multiple cooling cycles were done. The comparison of each measured variable is visible in Figure 36. The cooling cycle shown above is cycle 1. A very surprising cooling cycle is marked in blue. The LED did not emit light anymore. Why this is the case could not be determined, since this behavior did not occur a second time. The first suspicion was an electrical contact that lost its connection. This would mean that the forward voltage would increase to the maximum value the ADC can measure. As will be seen for the next LED, the ADC board can measure voltages up to 8 V and is therefore not saturated here (see Figure 36 (a)). The setup did also not change between those measurements. Apparently, the LED can have an unstable behavior at low temperatures. Cycle 1

and 3 in Figure 36 however, show a very similar behavior for all measured quantities. The qualitative characteristics stay the same as for the OP130, but even the quantities are very comparable. The largest relative difference between the normalized efficiency is about 4.2%. For the output power this value is approximately 3.2%. Even the peak of the FWHM at high temperatures is consistent for cycle 1 and 3 and can be seen in Figure 36 (e). Since the differences between cycles are reasonably small, it is deduced that the LED has a consistent behavior at the temperature range of $8\,\text{K} < T < 300\,\text{K}$. However, a failure of the LED can occur too. Whether this behavior is only true for this particular LED or for other ones of the same too, was not measured.

3.4   MTE4064NK2-UR

The MTE4064NK2-UR LED from Marktech Optoelectronics emits light with a wavelength of 650 nm [30]. The material composition is not given, but an assumption will be made later. The measuring procedure is the same as for the other two LEDs. The only difference is the length of the reduction tube (see Figure 12), which is approximately 2.5 cm.
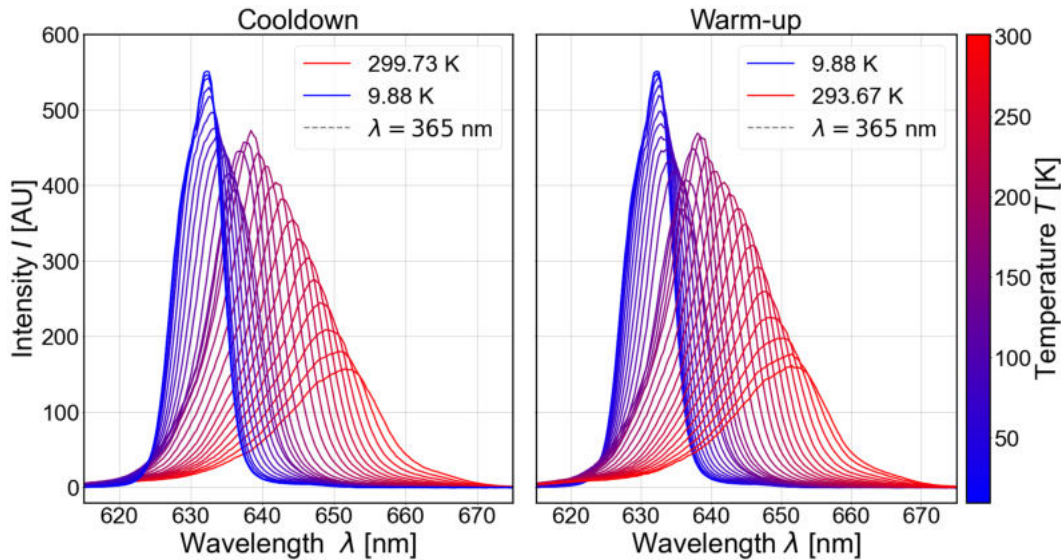

Figure 37: MTE4064NK2-UR: Measured spectra as a function of temperature, which is shown by the color of each spectrum. The visible plot show the cooldown (left) and the warm-up (right).

The chosen integration time is 3 ms with a time of 45 s between measurements, as for the OP232 LED. The spectra for cooldown and warm-up are shown in Figure 37. The temperature difference between each spectrum is 10 K. As expected, the peak wavelength starts at approximately 650 nm and shift to lower wavelengths as the temperature decreases. The intensity increases too, but then decreases and rises again, which is a new behavior of the spectrum. As before, first the peak position will be analysed.

Since the peak is sufficiently symmetrical, a parabolic fit $I(\lambda) = a \cdot (\lambda - b)^2 + c$ is possible for each spectrum. An example of such a peak fit is visible in the appendix (see Figure 53). The corresponding peak parameters can be found in Table 9 in the appendix. The errors are very large, as they were for the OP130 peak fit, but since the resulting peak positions make sense, it is assumed to be a good description of the spectrum peak. The resulting temperature dependence of the peak position is shown in Figure 38 (a). Over a range of about 300 K, the peak position changes by 19.6 nm. Above $T = 130$ K, the temperature dependency is almost linear with its maximum at $\lambda_{peak}^{max} = 651.5$ nm. The slope decreases for lower temperatures until the peak position reaches a minimum of $\lambda_{peak}^{min} = 631.9$ nm. The energy increase that occurs with a smaller wavelength seems to be similar to the energy band gap temperature dependence shown in the appendix (Figure 51). This suggests that this temperature dependence is the reason for the wavelength shift. The energy
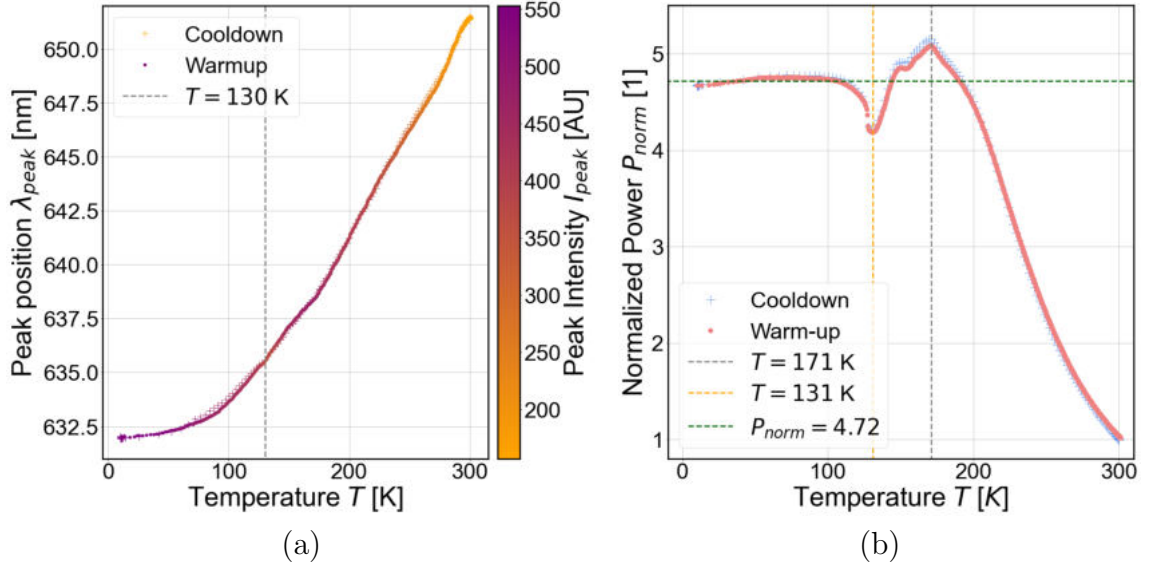
Figure 38: MTE4064NK2-UR: (a) Temperature dependence of the peak position. The corresponding peak intensity is shown by the color. (b) Normalized optical power as a function of temperature.

occupation might also change within the semiconductor, which could also have an effect on the peak wavelength. The dominant factor of both can not be determined here.

The optical output power is again calculated by summing over the intensity values in a certain range and normalize this sum. The selected range is 600 nm to 690 nm. The resulting temperature dependent power is shown in Figure 38 (b). For temperatures above 171 K, the power increases monotonously with decreasing temperature. A maximum is reached at 171 K. The following decrease between 171 K and 131 K is very irregular and shows parts that are very steep and others that are almost constant. The decrease ends at a local minimum at $T = 131$ K. Below this temperature, the normalized power rises to a nearly constant value of approximately 4.72 times the power output at room temperature. The power curve is surprising, as the other LEDs do not show such a behavior. To analyse it further, the peak intensity and FWHM are determined.

The FWHM is visible in Figure 39 (a). For comparison, the dashed lines at $T = 131$ K and 171 K show the positions of the maximum and the local minimum of the optical power (Figure 38 (b)). The FWHM decreases from 15.9 nm to a local minimum of 7.5 nm at 161 K. A local maximum is reached at approximately 131 K. For lower temperatures, the FWHM decreases further and reaches a minimum value of 7.4 nm at 9.88 K. This peak width behavior is opposite to what was expected, because the minimum and maximum are roughly at temperatures where the output power has a maximum and minimum, respectively. Thus, the peak intensity has to be responsible for this effect. Overall, the peak width decreases during cooldown, which corresponds to a larger state density in the semiconductor.

The peak intensity (see Figure 39 (b)) rises with decreasing temperature from starting value of 157 to a local maximum of 474 at $T = 167$ K. The power reaches its maximum at 171 K. This is close enough to be able to say that the power peak is
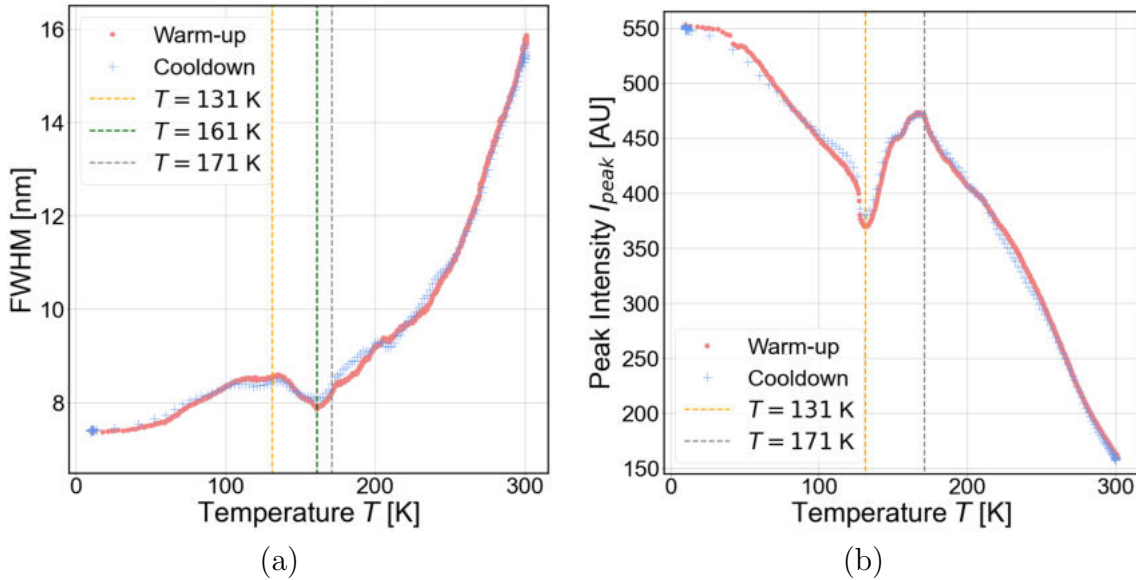
Figure 39: MTE4064NK2-UR: (a) Temperature dependence of the FWHM. (b) Peak intensity as a function of temperature.

a result of the peaking intensity. The same applies to the local minimum of the peak intensity, which has a value of 369 at $T = 131 \, \text{K}$. For temperatures lower than 131 K, the peak intensity rises monotonously to a maximum of 553 at 9.88 K. Regarding the power, the increase of the peak intensity and the decrease of the FWHM cancel each other out and result in a stable power output for low temperatures under 131 K. For higher temperatures, the intensity change of the peak is the dominant factor that increases the optical power of the diode. Associated physical effects could be the charge carrier concentration and the transparency of the material. If more charge carriers are able to emit photons, intensity of the peak gets higher. The same is true if more photons can escape the material as they are not absorbed.

The measured forward voltage is shown in Figure 40 (a). Its increase is not linear over the whole temperature range, but rises monotonically. The value at room temperature is about 1.98 V. The maximum value is 8.35 V, which is reached at 9.88 K. The maximum voltage is unexpectedly high and could be the result of a larger energy band gap or an occupation of low energy levels in the conduction band. The reason cannot be analysed any further with the used setup. The normalized electrical input power is shown Figure 40 (b). It has no significant difference to the forward voltage, which is expected as the current is not changing a lot.

Now that the input and output power is given, the efficiency can be calculated. The normalized efficiency is visible in Figure 41, which has a value of 1 at room temperature. With colder temperatures, it rises almost linearly until reaching a maximum efficiency of $\nu_{norm}^{max} = 2.6$ times its starting value. This maximum is at approximately $T = 190 \, \text{K}$. For temperatures under 190 K, the efficiency decreases with a local minimum at around 129 K. The decreases beneath that temperature is less steep until it reaches a value of 1.23 times the efficiency at room temperature at 9.88 K. This behavior can be explained when looking at the input and output power. For high temperatures above 190 K, the electrical power and the optical power both rise, with the latter having a more steep increase. This is why the efficiency rises at
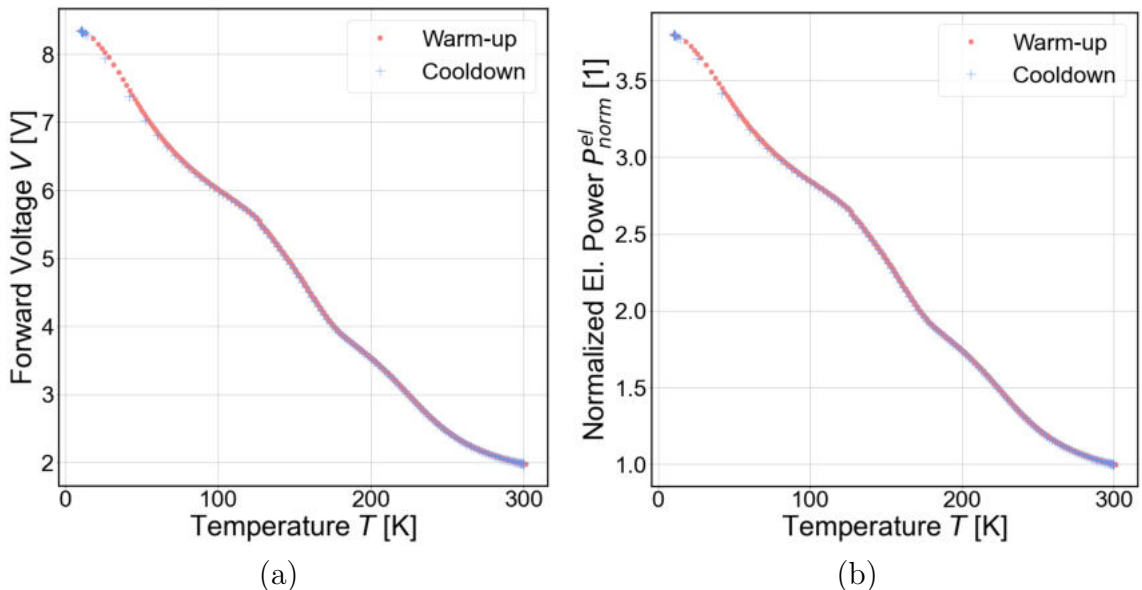
Figure 40: MTE4064NK2-UR: (a) Forward voltage as a function of temperature. (b) Temperature dependency of the normalized electrical input power.

these temperatures. The output power has its maximum at 171 K, which is where the steep decrease of the efficiency begins, which is a result of the rising input power and decreasing output power. At 131 K, the optical power reaches its local minimum, which corresponds to the efficiency minimum at $T = 129$ K. Since the output power is almost constant for lower temperatures and the input power still increases, the efficiency decreases. An efficiency decline of this magnitude was not seen for the other LEDs. The reason is the very high forward voltage that is required to power the LED at low temperatures, which corresponds to a large energy band gap. Since the output power is the most important characteristic for the OSEM, this LED shows a very stable optical power source under 100 K. Whether this is the case for different cooling cycles will be analysed below.

As seen in Figure 42, the LED shows very similar behavior for different cooling cycles. The forward voltage (Figure 42 (a)), electrical power (Figure 42 (c)) and FWHM (Figure 42 (e)) are so equal that they can be barely distinguished from each other. A difference occurs in the optical output power, which is shown in Figure 42 (b). One cooling cycle had significantly different power output values for temperatures below 240 K. This is the temperature where the relative difference between cycle 1 and 2 exceeds 5%. As a result of the discrepancy, the efficiency of cycle 1 differs significantly too (see Figure 42 (d). The peak intensity also shows variations for different cycles. Here, cycle 3 seems to be the one with the most deviation. The relative difference between cycle 1 and 3 is 9.6% at the lowest temperature of 9.84 K. Although there are some differences between multiple cooling cycles, the qualitative behavior of the LED stays the same. The mentioned maxima and minima occur in all of these measurements. It is concluded that the LED MTE4064NK2-UR from Marktech Optoelectronics is useful for devices at low temperatures under 40 K, since it has a stable power output.

Since the LEDs material composition is not known, it can be guessed by the wavelength the diode emits at room temperature. Phtotons with a wavelength of

650 nm have an energy of about $E = hc/\lambda = 1.9\,\text{eV}$. Therefore, the energy band gap at room temperature should be in this range. Since E_g depends on the specific doping of the material a certain material can not be determined here. According to [31], gallium phosphide (GaP) has an energy band gap of about $2.26\,\text{eV}$. Since no gallium based composition was found that is closer to the photon energy emitted by the semiconductor and the dependence on doping could change this value significantly, GaP is the most likely choice of material for the MTE4064NK2-UR.
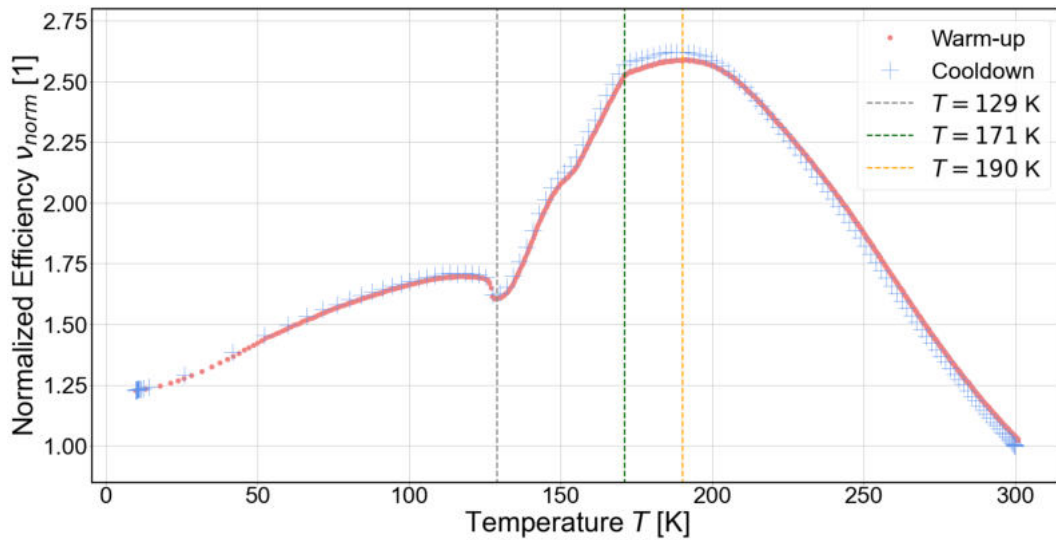
Figure 41: Temperature dependence of the efficiency of an MTE4064NK2-UR.
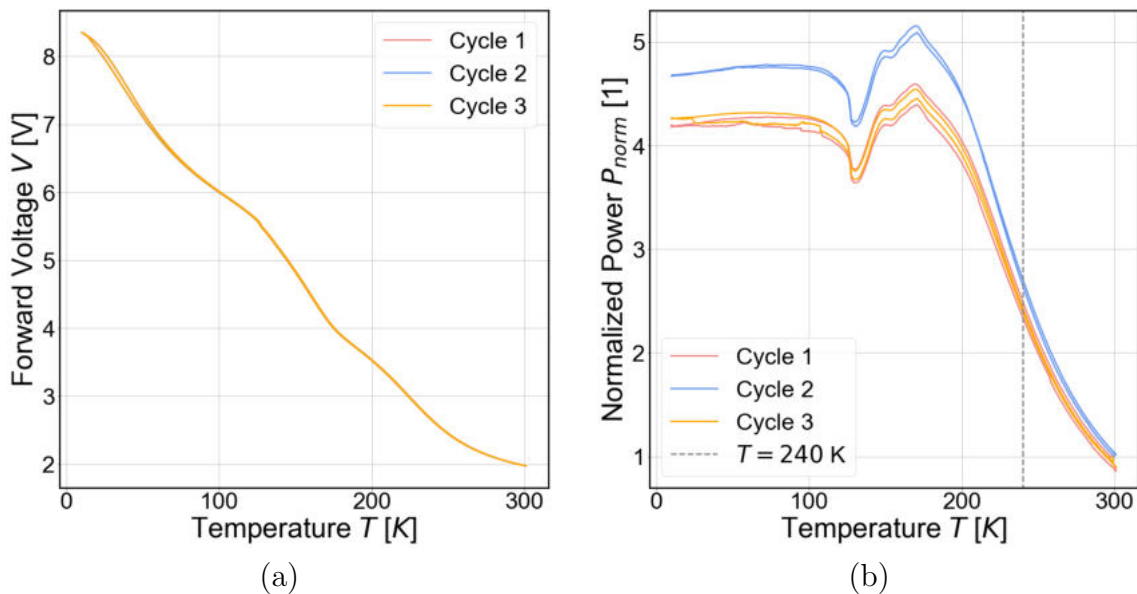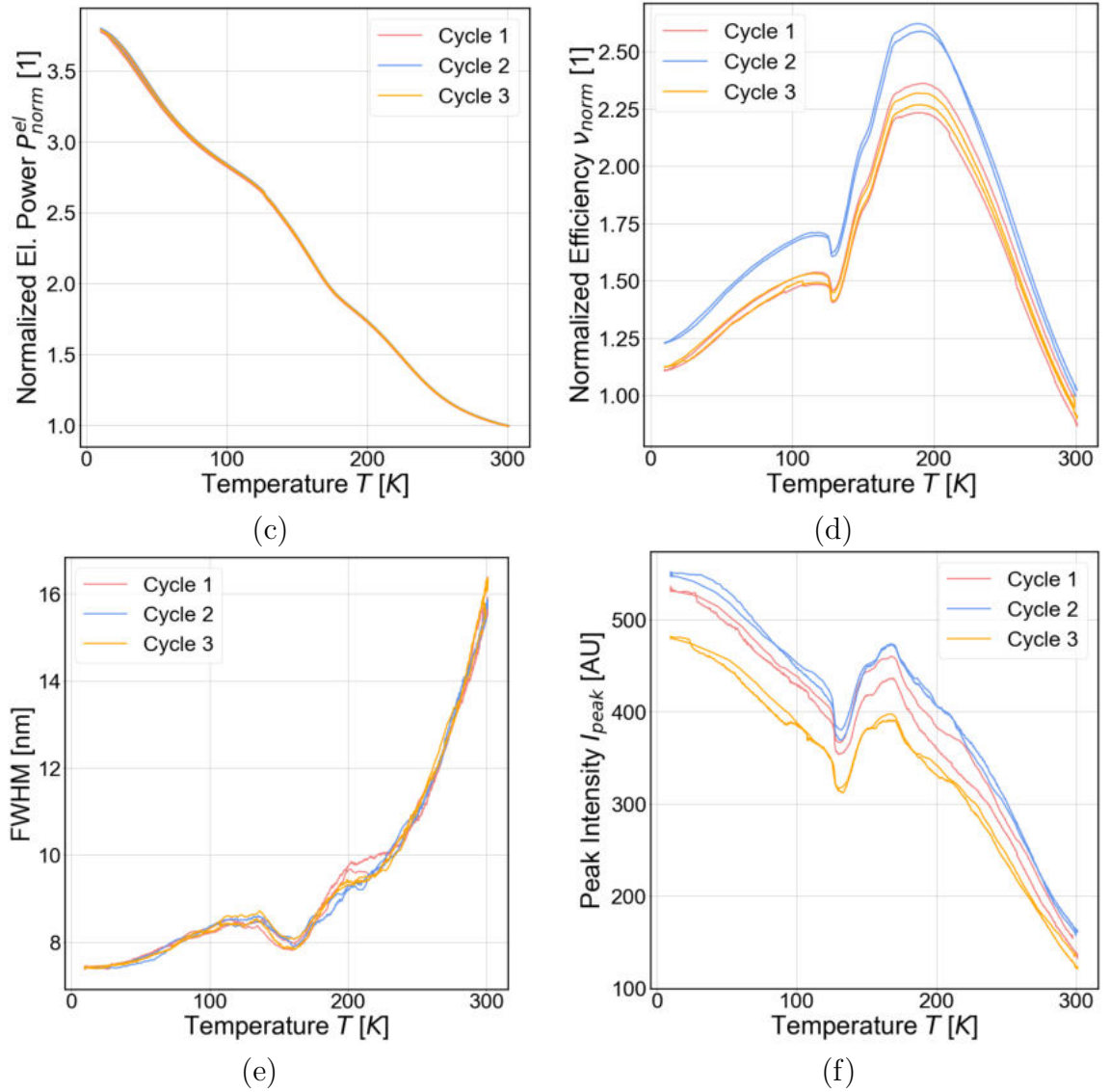
Figure 42: Comparison of three different cooling cycles of (a) the forward voltage, (b) the opitcal power output, (c) the electrical input power, (d) the efficiency of the diode, (e) the FWHM and (f) the maximum intensity of an MTE4064NK2-UR.

3.5   Conclusion

The goal of this thesis is the analysis of the temperature dependence of diodes. This is done by cooling them down to cryogenic temperature and measuring their spectrum and forward voltage during cooldown and warm-up. Before testing the LEDs, it is necessary to calibrate the spectrometer, the current source and the ADC board, which measures the forward voltage.

The first LED that was cooled down is the gallium arsenide OP130 from TT Electronics. It is set to be a 935 nm LED, which could not be confirmed due to the measured peak wavelength of 912 nm. It shows a for gallium based semiconductors typical voltage behavior and a monotonous increase in optical power with decreasing temperature. The efficiency increases approximately by a factor of 6 compared to operation at room temperature. Although it is probably a result of the LED mounting, it should be noted that the measurements showed broad differences for different cooling cycles especially regarding the output power.

The OP232 from TT Electronics is a 890 nm LED made of gallium aluminium arsenide. It shows a stable wavelength and optical power behavior under 40 K and also has the typical temperature dependency of the forward voltage mentioned above. The differences between cooling cycles are reasonably small, whereby the LED did not emit any light at low temperatures during one measurement.

The last measured diode is the MTE4064NKN2-UR from Marktech Optoelectronics. It is a 650 nm LED that has a much larger forward voltage at low temperatures than the other ones with a maximum value over 8 V. Its output power shows a stable behavior under 100 K, but maxima and minima for higher temperatures. For different cooling cycles, the fluctuations are not large with a maximum relative difference of the efficiency under 10%.

It is important to notice that only one LED of each type was analysed. Whether these characteristics are the same for all LEDs of this type or if there are more fluctuations in their behavior was not determined. To further improve the reproducibility of the results, this would be the first step. The results can now be used to have a good understanding of an LEDs behavior in the temperature range from 10 K to 300 K for devices like the OSEM, which this thesis is done for.

References

1. Abbott, B. P. *et al. Observation of Gravitational Waves from a Binary Black Hole Merger* 2016.

2. Akutsu, T. *et al.* Compact integrated optical sensors and electromagnetic actuators for vibration isolation systems in the gravitational-wave detector KAGRA. *The Review of scientific instruments* **91,** 115001 (2020).

3. Thorne, K. S. *Gravitational Waves* 1995. https://arxiv.org/pdf/gr-qc/9506086.

4. Fryer, C. L. & New, K. C. B. Gravitational Waves from Gravitational Collapse. *Living reviews in relativity* **14,** 1. ISSN: 1433-8351 (2011).

5. Chris L. Fryer and Kimberly C. B. New. Gravitational Waves from Gravitational Collapse (2011).

6. *LIGO's Interferometer — LIGO Lab — Caltech* 29.07.2022. https://www.ligo.caltech.edu/page/ligos-ifo.

7. McClelland, D. *et al. 3G R&D: R&D for the Next Generation of Ground-based Gravitational-wave Detectors* http://arxiv.org/pdf/2111.06991v1.

8. Abbott, B. *et al.* Search for gravitational-wave bursts in LIGO data from the fourth science run. **24,** 5343–5369 (2007).

9. ET Steering Committee Editorial Team. *Design Report Update 2020 for the Einstein Telescope* 2020.

10. Hild, S. *et al.* Sensitivity studies for third-generation gravitational wave observatories. *Classical and Quantum Gravity* **28,** 094013. ISSN: 0264-9381. http://arxiv.org/pdf/1012.0908v1 (2011).

11. *Instrumentation reference book* 3rd ed. ISBN: 9780080478531. https://ebookcentral.proquest.com/lib/kxp/detail.action?docID=294192 (Butterworth-Heinemann, Boston, 2003).

12. Stuart, A. BOSEM Design Document & Test Report (2014).

13. *Hermetic Infrared Diode: OP130 Series* 2019. https://www.ttelectronics.com/TTElectronics/media/ProductFiles/Datasheets/OP130.pdf.

14. *Advanced Photonix: LS-0505 Series* 2018. https://media.digikey.com/pdf/Data%20Sheets/Photonic%20Detetectors%20Inc%20PDFs/LS-0505-XX.pdf.

15. Othmar Marti und Alfred Plettl. *Vorlesungsskript Physikalische Elektronik und Messtechnik Bachelor Physik* 2018. http://wwwex.physik.uni-ulm.de/lehre/physikalischeelektronik/phys_elektr/phys_elektr.pdf.

16. Stiny, L. *Aktive elektronische Bauelemente* ISBN: 978-3-658-14386-2 (Springer Fachmedien Wiesbaden, Wiesbaden, 2016).

17. W. Shockley. The Theory of p-n Junctions in Semiconductors and p-n Junction Transistors. *Bell System Technical Journal* **28,** 435–489. ISSN: 00058580 (1949).

18. Olav Torheim. *Elememtary Physics of P-N-junctions* 2007. https://web.archive.org/web/20120210214029/http://web.ift.uib.no/~torheim/pnsjikt.pdf.

19. Abdelrahman Mohammed Attia. *P-N Junction* 2020.

20. Lutz, J. *Halbleiter-Leistungsbauelemente* ISBN: 978-3-642-29795-3 (Springer Berlin Heidelberg, Berlin, Heidelberg, 2012).

21. Isamu Akasaki, Hiroshi Amano, Shuji Nakamura. *The Nobel Prize in Physics 2014: Blue LEDs - Filling the world with new light* 2014.

22. Robert Joppe. *Personal Conversation* 2.11.2022.

23. Lisk, A. Red Tide USB650 Fiber Optic Spectrometer Installation and Operation Manual.

24. Kramida, A., Ralchenko, Y., Reader, J., Team & ASD, N. 2022. `https://physics.nist.gov/asd`.

25. Agilent Technologies. *Porduct Overview* 2007. `https://www.alldatasheet.com/datasheet-pdf/pdf/884095/HP/34401A.html`.

26. *SONY ILX511 Data Sheet* `https://pdf1.alldatasheet.com/datasheet-pdf/view/47492/SONY/ILX511.html`.

27. Meyaard, D. S. *et al.* Analysis of the temperature dependence of the forward voltage characteristics of GaInN light-emitting diodes. *Applied Physics Letters* **103,** 121103. ISSN: 0003-6951 (2013).

28. *Hermetic Infrared Emitting Diode: OP230 Series* 2022. `https://www.ttelectronics.com/TTElectronics/media/ProductFiles/Datasheets/OP230.pdf`.

29. O'Donnell, K. P. & Chen, X. Temperature dependence of semiconductor band gaps. *Applied Physics Letters* **58,** 2924–2926. ISSN: 0003-6951 (1991).

30. *Visible Emitter: MTE4064NK2-UR* 2016. `https://www.marktechopto.com/pdf/products/datasheet/MTE4064NK2-UR.pdf`.

31. *Semiconductor Materials - Table of Semiconductor Materials — Table Semiconductor Materials* 20.11.2022. `https://www.liquisearch.com/semiconductor_materials/table_of_semiconductor_materials`.

A   Setup and Calibration

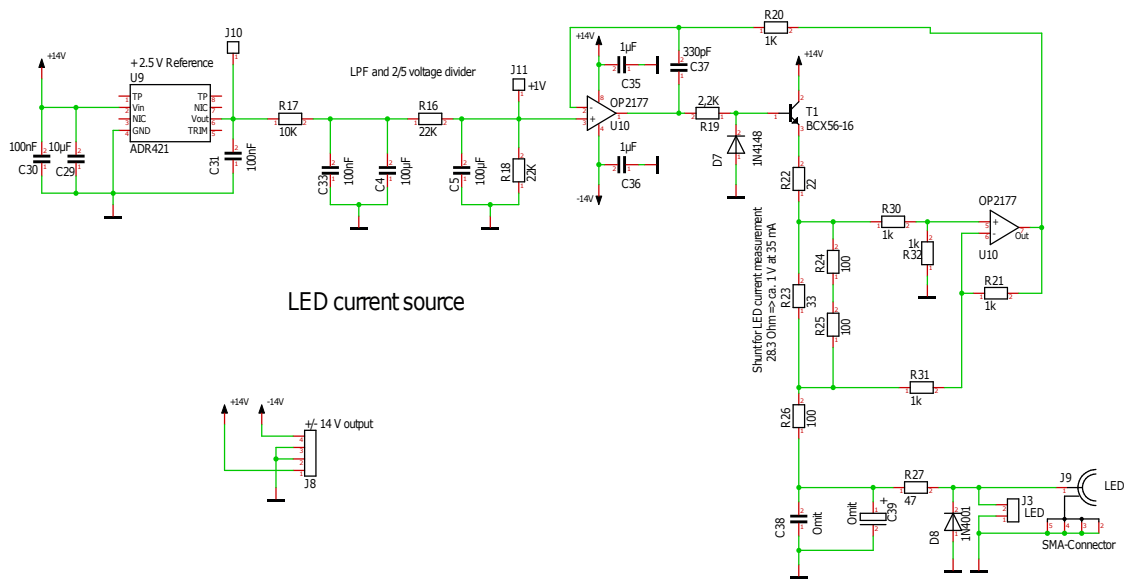## A.1   LED Current Source

LED current source

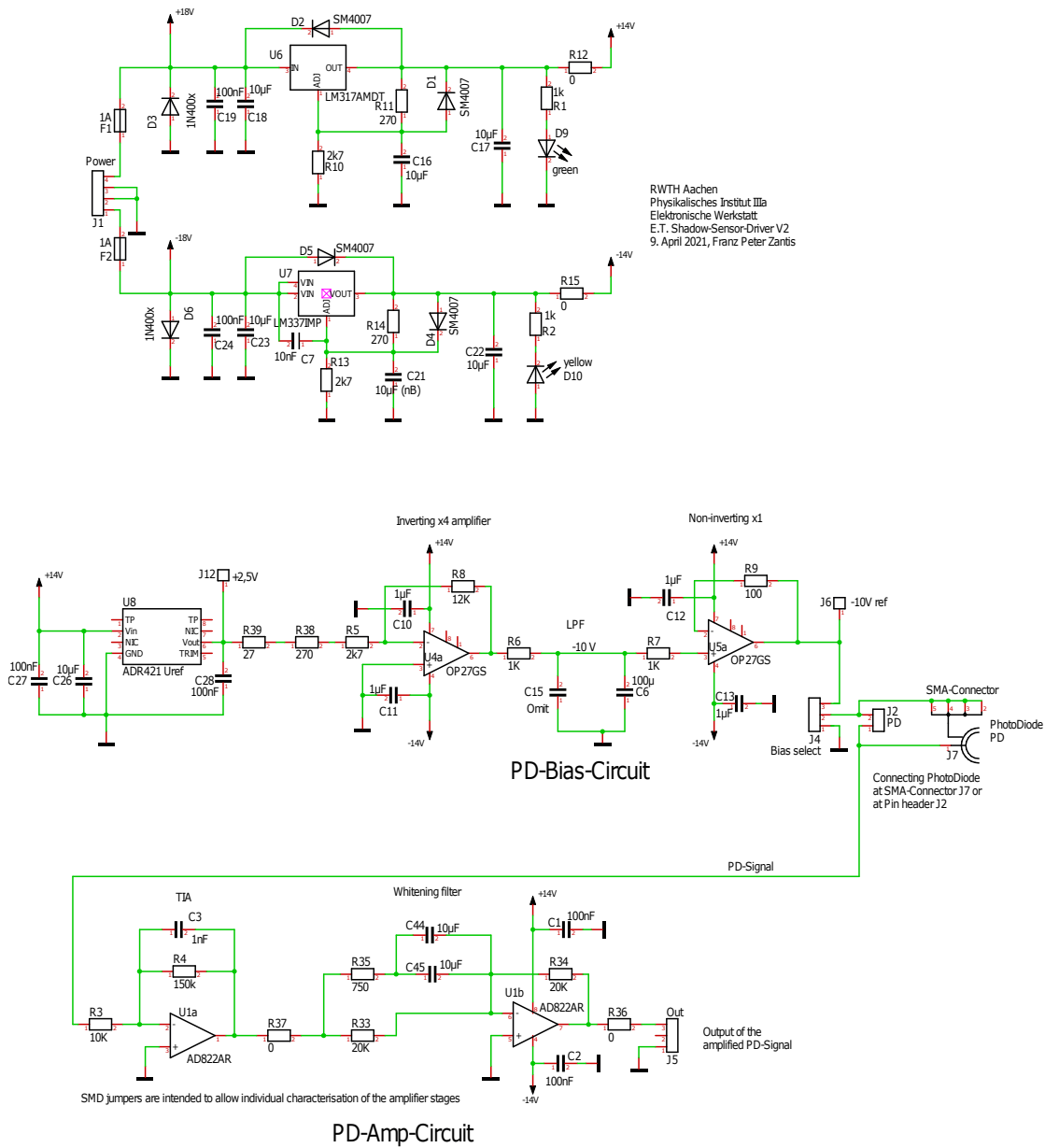Figure 43: Current source layout part 1.

Figure 44: Current source layout part 2.

A.2   Calibration
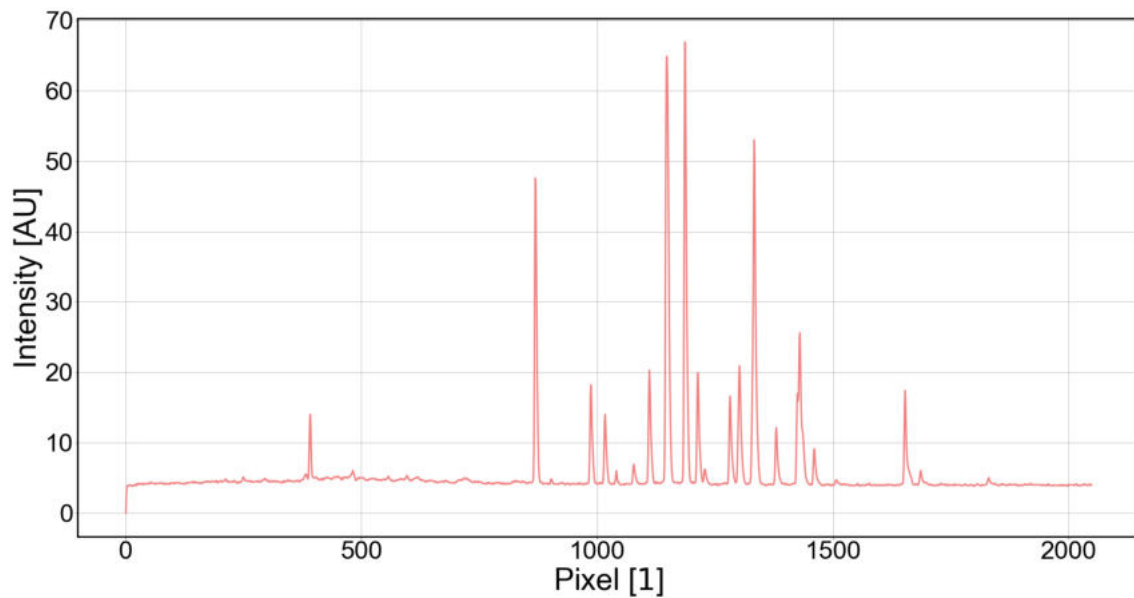
A.2.1   Spectrometer

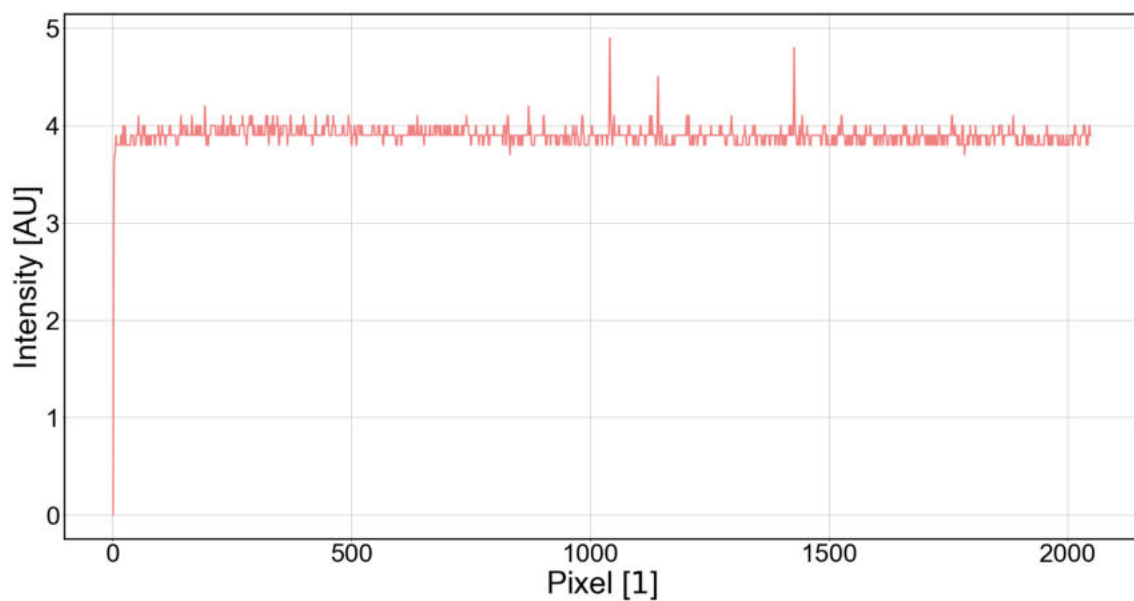Figure 45: Raw argon spectrum used for the spectrometer calibration.
.

Figure 46: Raw offset measurement for the offset determination of the spectrometer.

	$a \pm \sigma_{a,stat}$	$b \pm \sigma_{b,stat}$	$c \pm \sigma_{c,stat}$	χ^2/N_{dof}	$\lambda_{lit} \pm \sigma_{\lambda_{lit}}$ [nm]
1	-1.21 ± 0.28	391.74 ± 0.16	10.17 ± 0.21	0.142	$488.90422 \pm 2e-05$
2	-1.46 ± 0.32	986.96 ± 0.17	14.30 ± 0.05	0.191	$696.54307 \pm 2e-05$
3	-1.01 ± 0.22	1016.95 ± 0.17	10.10 ± 0.05	0.206	$706.72181 \pm 2e-05$
4	-1.72 ± 0.37	1111.03 ± 0.17	16.40 ± 0.05	0.189	$738.39805 \pm 2e-05$
5	-2.02 ± 0.34	1148.00 ± 0.16	61.00 ± 0.03	0.843	$750.38691 \pm 3e-05$
6	-5.78 ± 1.45	1186.60 ± 0.16	64.33 ± 1.47	0.471	$763.5106 \pm 2e-05$
7	-1.48 ± 0.36	1213.66 ± 0.16	16.19 ± 0.34	0.343	$772.37611 \pm 2e-05$
8	-1.28 ± 0.28	1282.06 ± 0.17	12.70 ± 0.06	0.139	$794.81764 \pm 3e-05$
9	-1.15 ± 0.19	1302.07 ± 0.16	17.10 ± 0.06	0.406	$801.47857 \pm 3e-05$
10	-3.84 ± 0.98	1333.31 ± 0.20	49.42 ± 0.72	0.564	$811.5311 \pm 3e-05$
11	-0.69 ± 0.12	1380.00 ± 0.16	8.20 ± 0.03	1.1	$826.45225 \pm 3e-05$
12	-0.93 ± 0.22	1425.22 ± 0.17	13.17 ± 0.19	2.624	$840.82096 \pm 3e-05$
13	-1.84 ± 0.42	1429.75 ± 0.16	21.80 ± 0.31	0.153	$842.46475 \pm 3e-05$
14	-0.48 ± 0.09	1460.55 ± 0.14	5.41 ± 0.12	0.174	$852.14422 \pm 3e-05$
15	-1.54 ± 0.34	1653.13 ± 0.17	13.52 ± 0.14	0.077	$912.29674 \pm 3e-05$

Table 8: Fit parameters of the parabola for each pixel. The left column describes the peak number, while the peak position is given by b. λ_{lit} is the literature wavelength of the argon peaks.
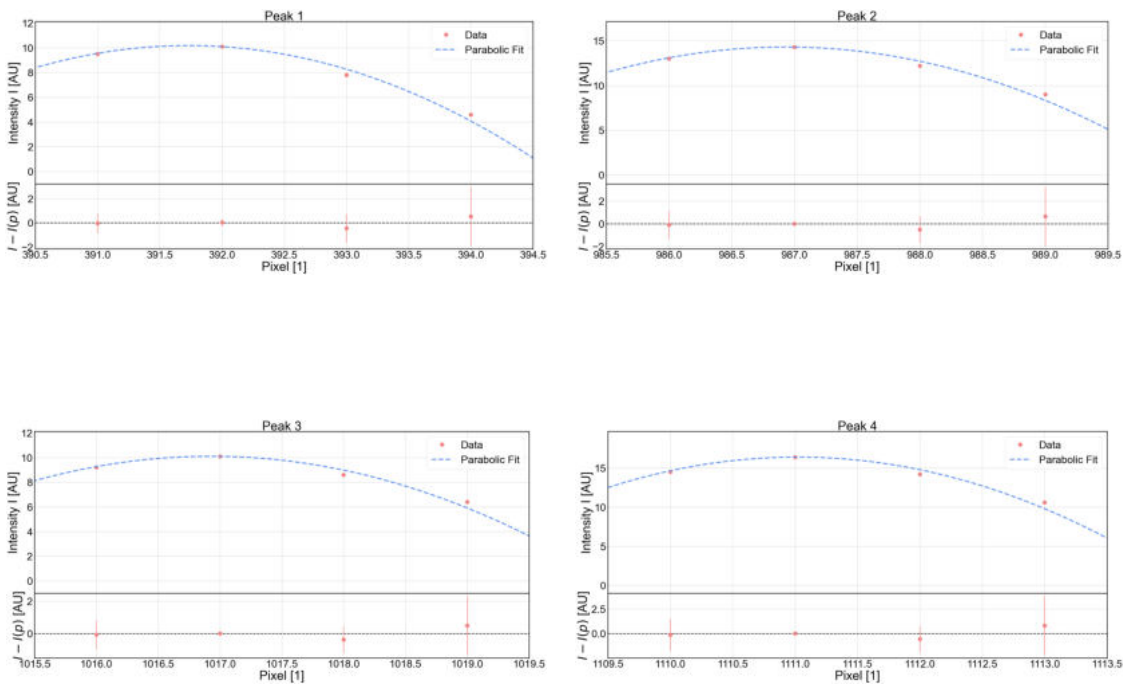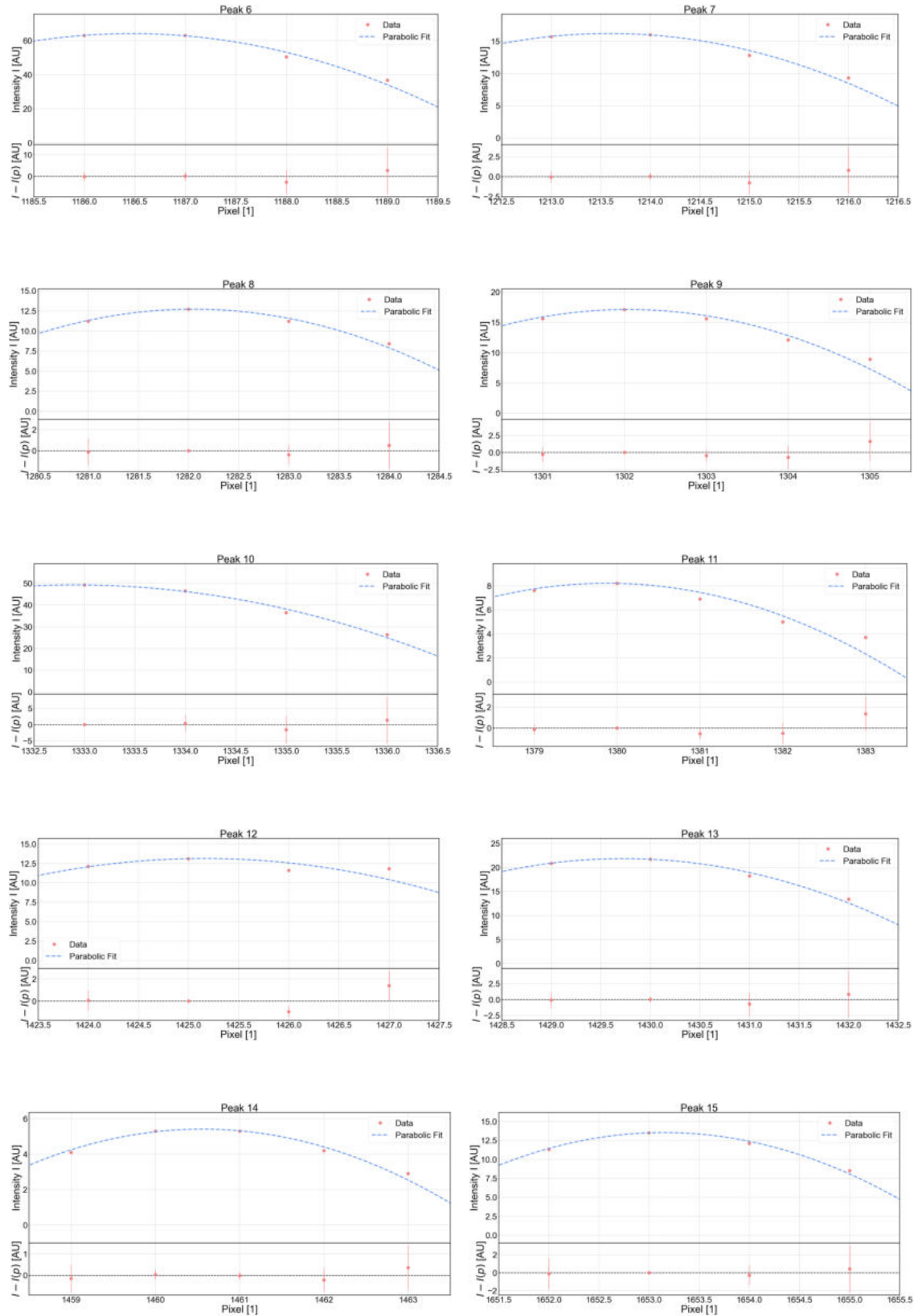
Figure 47: Peak fits of all 15 argon peaks used for the spectrometer calibration.
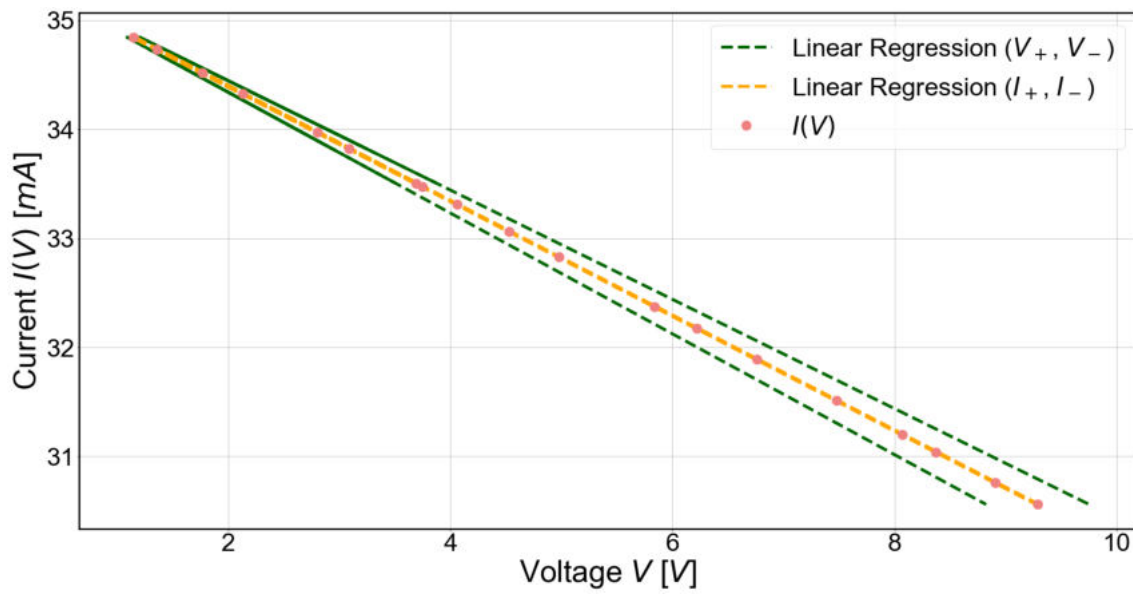
A.2.2   Current Source

Figure 48: Shift method for the current source calibration.

B   Analysis

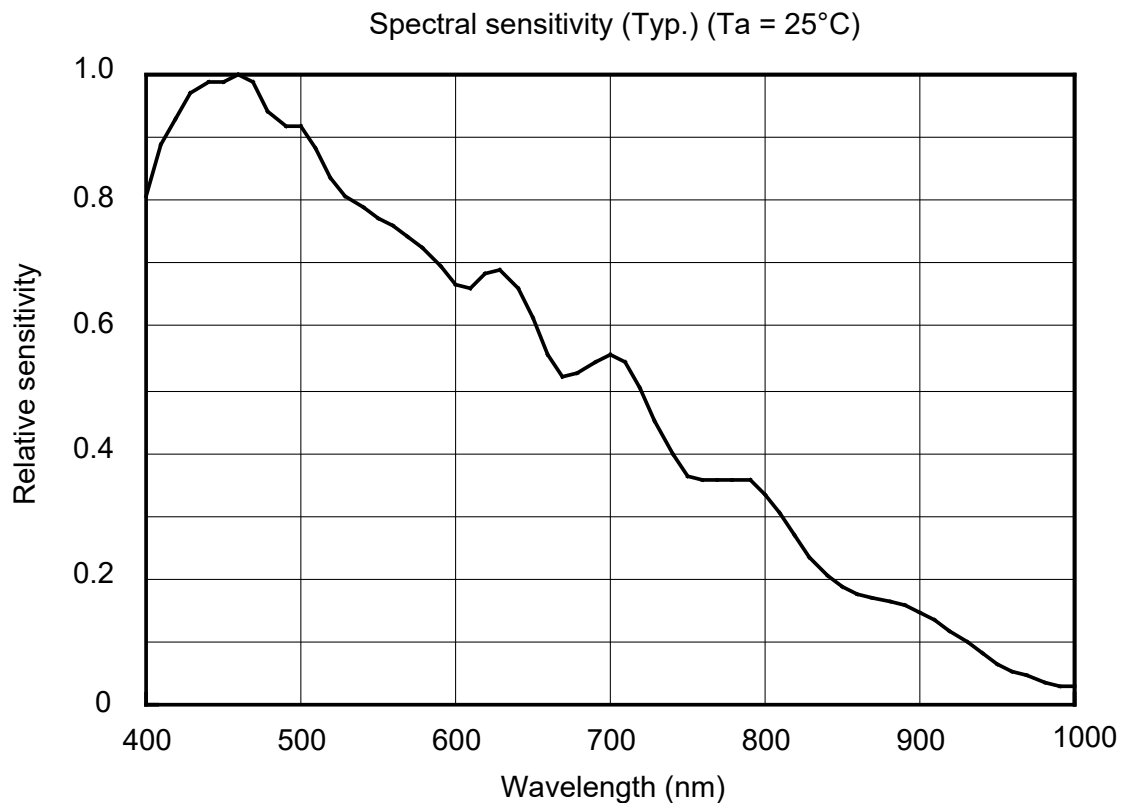## B.1   Spectral Sensitivity

Spectral sensitivity (Typ.) (Ta = 25°C)
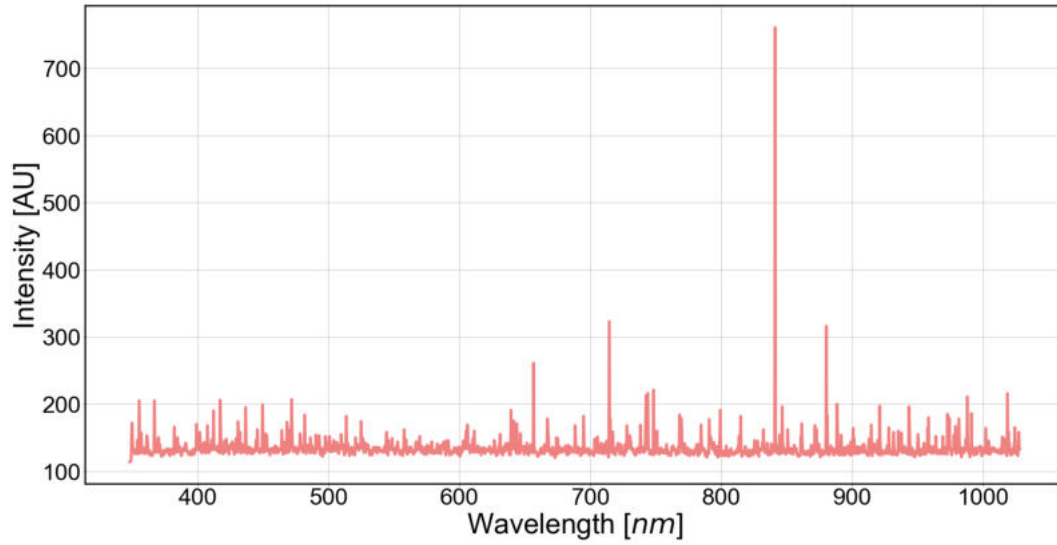
Figure 49: Spectral sensitivity taken from [26]

Figure 50: Dark noise measurement with integration time of 1000 ms. Multiple hot pixel are visible.
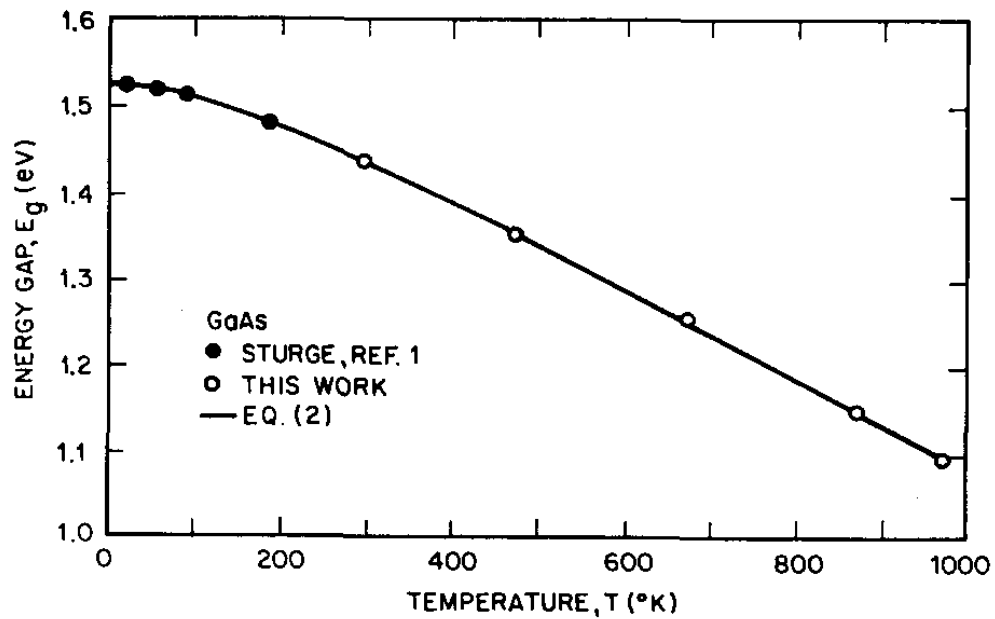
B.2   OP130

Figure 51: Temperature dependence of GaAs band gap energy from [29].
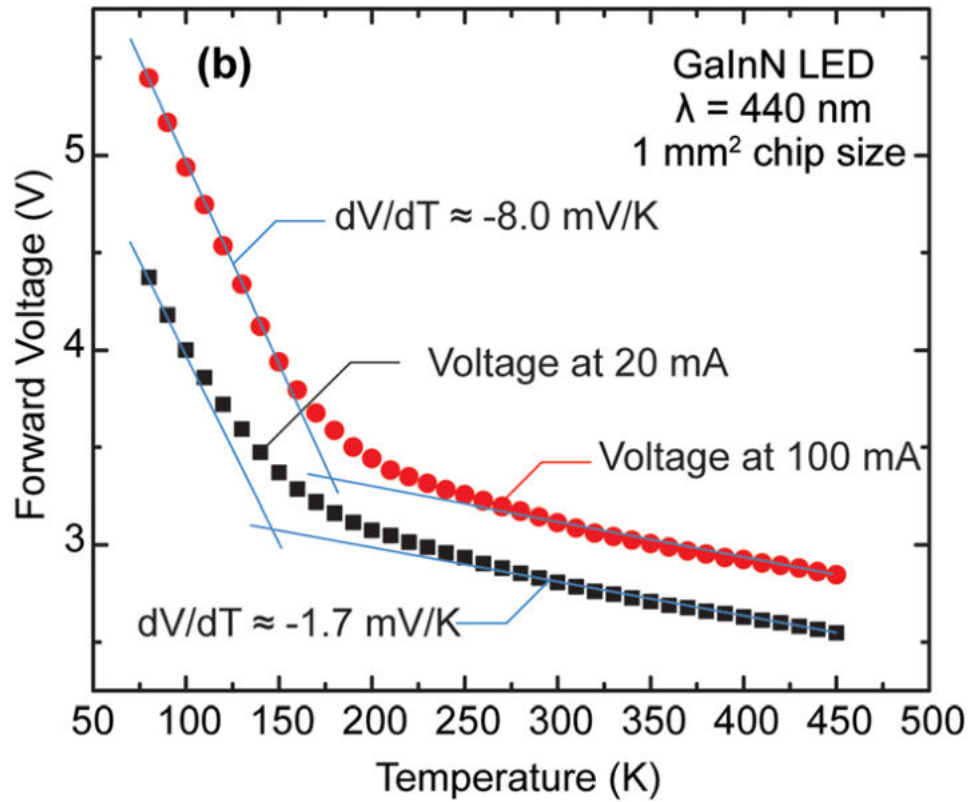
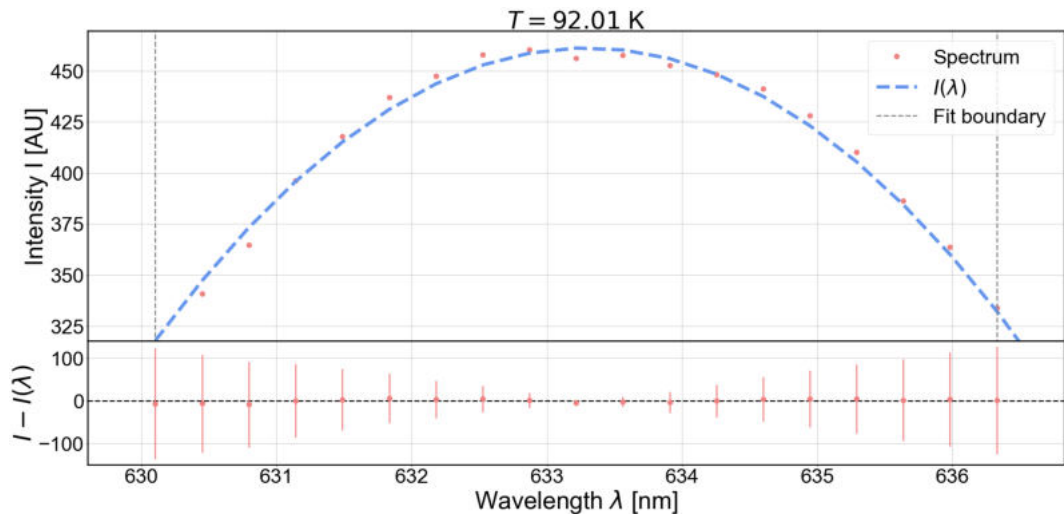Figure 52: Temperature dependence of forward voltage [27].

B.3   MTE4064NK2-UR

Figure 53: Example of a peak approximation at $T = 92.01 \, \text{K}$ and its residual plot. Since the errors are very large, the χ^2/N_{dof} is with 3 very small.

$a \pm \sigma_{a,stat}$	$b \pm \sigma_{b,stat}$	$c \pm \sigma_{c,stat}$	χ^2/N_{dof}
-14.044 ± 3.755	633.30 ± 0.23	461.17 ± 5.66	0.034

Table 9: Fit parameters for the peak shown in Figure 53